Eddy Variability and Energetics from Direct Current Measurements in the Antarctic Circumpolar Current South of Australia

HELEN E. PHILLIPS*

Institute of Antarctic and Southern Ocean Studies, University of Tasmania, Hobart, Tasmania, Australia

STEPHEN R. RINTOUL

Antarctic Cooperative Research Centre, and CSIRO Division of Marine Research, Hobart, Tasmania, Australia

ABSTRACT

Two-year time series measurements of current velocity and temperature in the Subantarctic Front (SAF) south of Australia from 1993 to 1995 provide estimates of eddy fluxes of heat and momentum across the Antarctic Circumpolar Current (ACC) and further insight into the variability of the ACC. The SAF was found to be an energetic, meandering jet with vertically coherent fluctuations varying on a timescale of 20 days with typical amplitude 30 cm s^{-1} at 1150 dbar. A daily varying coordinate frame that follows the direction of flow allowed mesoscale variability of the SAF to be isolated from variability due to meandering of the front and proved very successful for examining eddy fluxes. Vertically averaged cross-stream eddy heat flux was 11.3 kW m^{-2} poleward and significantly different from zero at 95% for fluctuations in the 2–90 day band. Zonally integrated, this eddy heat flux (=0.9 PW) is more than large enough to balance heat lost south of the Polar Front and is as large as cross-SAF fluxes found in Drake Passage. Cross-stream eddy momentum fluxes were small, not significantly different from zero, and of indeterminate sign, but tending to decelerate the mean flow. A relationship between vertical motion and meander phase identified in the Gulf Stream was found to hold for the ACC. Eddy kinetic energy levels were similar to those in Drake Passage and southeast of New Zealand. Eddy potential energy was up to an order of magnitude larger than at other ACC sites, most likely because meandering of the front is more common here. Baroclinic conversion was found to be the dominant mechanism by which eddies grow south of Australia. Typical eddy growth time is estimated to be 30 days, approximately twice as fast as in Drake Passage, consistent with eddy energy growing rapidly downstream.

1. Introduction

Long-term, in situ measurements of velocity and temperature in the Antarctic Circumpolar Current (ACC) have been concentrated in Drake Passage where the ACC is confined and where its limits can be clearly defined (Bryden 1979; Sciremammano 1980; Nowlin et al. 1985). The only other such measurements were made southeast of New Zealand away from geographical constrictions but where the ACC is still very energetic (Bryden and Heath 1985). The observations from these two locations have provided considerable insight into the

dynamics and thermodynamics of the ACC, but it is still unclear how representative these results are of the remainder of the 20 000 km long ACC where energy levels are often considerably less.

To address this question, and others, a third location in the ACC has been recently monitored with an array of four tall current meter moorings south of Australia, the AUSSAF array (Fig. 1). The location is a choke point for the ACC, but not a tight one, and satellite altimeter maps of velocity variance have shown it to be a region of low but growing eddy energy (Morrow et al. 1994). The location was chosen to satisfy two criteria. First, to be more representative of the remainder of the ACC than are Drake Passage and southeast of New Zealand. Second, to have sufficient eddy variability that the role of eddies in the dynamics of the ACC could be further examined. The array was positioned so as to be centered on the strongest jet of the ACC, which is the Subantarctic Front (SAF) south of Australia.

Eddies are thought to play two major roles in the

---

* Current affiliation: Woods Hole Oceanographic Institution, Woods Hole, Massachusetts.

Corresponding author address: Ms Helen E. Phillips, Woods Hole Oceanographic Institution, Mail Stop 21, 360 Woods Hole Road, Woods Hole, MA 02543.
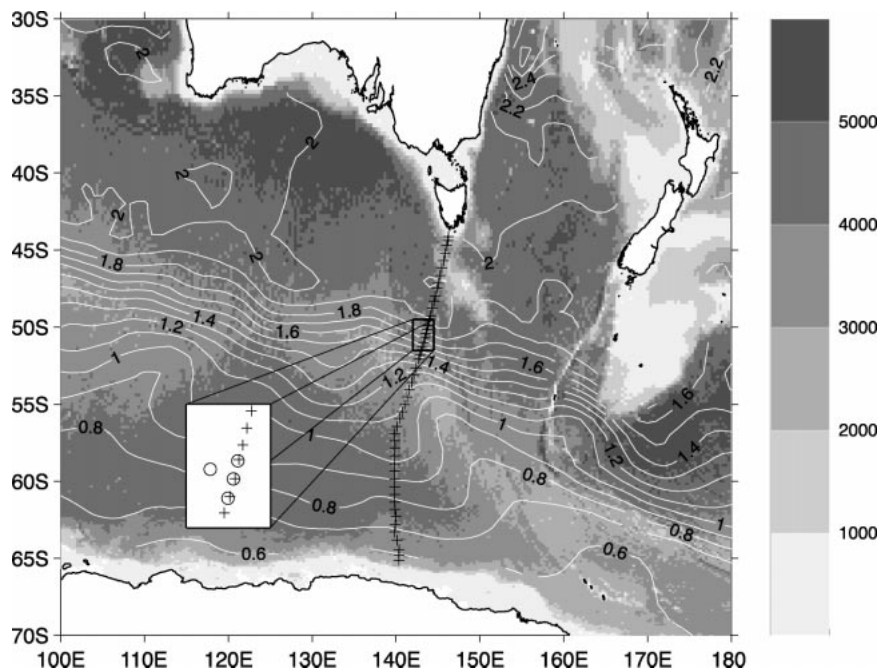E-mail: helen_ep@hotmail.com

FIG. 1. Location of the AUSSAF current meter array (circles inside box) and the WOCE SR3 hydrographic section (plus signs), overlaid on shading of Smith and Sandwell (1994) bathymetry in meters and contours of 0–2000 dbar dynamic height (dyn m) from Olbers et al. (1992). Box is expanded in Fig. 2.

ACC. The first is the transport of heat across the ACC to polar waters where it can balance heat lost there to the atmosphere. The heat balance for the Southern Ocean as written by Nowlin and Klinck (1986)

$$Q = F_g + F_{Ek} + F_e + F_{bc} \qquad (1)$$

says that the sum of ocean to atmosphere heat exchanges, Q, is balanced by the sum of F_g the heat flux by mean geostrophic flow excluding boundary currents, F_{Ek} the heat flux by surface Ekman transport, F_e the eddy heat flux, and F_{bc} the heat transport by deep boundary currents. The heat loss by the ocean Q has been estimated by Gordon [1985, personal communication as reported by de Szoeke and Levine (1981)] to be 3×10^{14} W $\pm 30\%$–50%, F_g was shown to be zero (de Szoeke and Levine 1981) but with large worst case errors of order 1×10^{14} W, and F_{Ek} is estimated to be 1.5×10^{14} W equatorward $\pm 50\%$ (de Szoeke and Levine 1981). The remaining terms, F_e and F_{bc}, must therefore account for 4.5×10^{14} W of poleward heat transport. There are no estimates to date of transport by deep boundary currents, but the two existing ACC studies have shown that the contribution made by eddies at these sites is poleward and is large enough to account for all of the required heat flux.

The second aspect of ACC dynamics thought to be affected by the mesoscale eddy field is the momentum balance of the ACC. Gill (1968) calculated that to balance the momentum added to the ACC by the strong zonal wind stress would require a meridional flux of

zonal momentum of order 100 cm² s⁻² on the northern and southern edges of the current. No significant meridional eddy momentum fluxes were observed in Drake Passage (Bryden 1979), while southeast of New Zealand, significant momentum fluxes were found but their magnitude was only 25% of that required to balance the wind stress. Morrow et al. (1994), using satellite altimeter measurements, found zonally averaged meridional flux of zonal momentum two orders of magnitude too small to balance the wind, and convergent on the mean flow. While lateral divergence of eddy momentum flux does not appear to be significant to the momentum balance of the ACC, eddies have been shown to transfer momentum vertically, by interfacial form drag, to the seafloor where it can be dissipated by bottom form stress (Johnson and Bryden 1989). The balance between wind stress and bottom form stress was originally proposed by Munk and Palmén (1951) and has since been confirmed in a variety of numerical models (e.g., McWilliams et al. 1978; Treguier and McWilliams 1990; Wolff et al. 1991; Stevens and Ivchenko 1997; Gille 1997).

The present paper uses the AUSSAF data to examine the vertical and horizontal structure of the SAF south of Australia, both in an Eulerian frame and in coordinates that follow the daily change in orientation of the front. Eddy fluxes of heat and momentum across the SAF are estimated and the distribution of eddy energy is determined. This paper is intended as a companion to the earlier ACC studies reporting similar observations
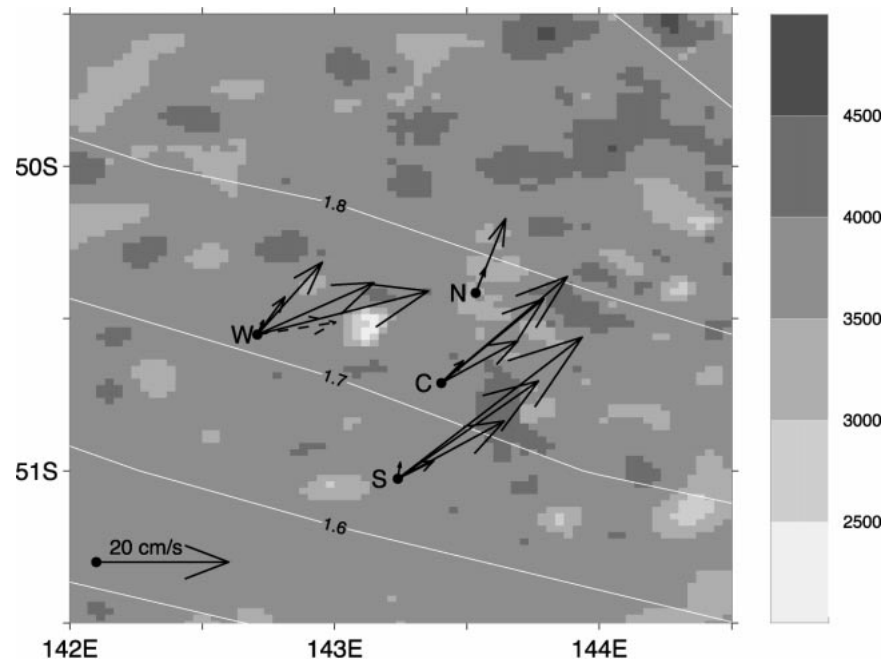
FIG. 2. Expansion of mooring location details in Fig. 1 with mean velocity vectors from each current meter. Strongest velocities correspond to shallowest instruments: 420 dbar on West, Central, and South, 1150 dbar on North. Means are full record length except at West where the common length of 132 days is used so that rotation of horizontal velocity with depth is not distorted. Velocity at West 1150 dbar is also shown for full record length (dashed vector) for comparison with other moorings. Contours are 0–2000 m dynamic height (dyn m) from Olbers et al. (1992).

from Drake Passage (Bryden 1979; Sciremammano 1980; Nowlin et al. 1985) and southeast of New Zealand (Bryden and Heath 1985). The location of the current meter array southeast of New Zealand relative to the ACC is similar to that for AUSSAF: close to, and for a large part of the deployment in, the SAF. The Drake Passage measurements are from the 1975–80 International Southern Ocean Studies (ISOS) current meter arrays, which either fully spanned the passage or were located midpassage. There is good coverage for the whole passage near 2700 m, but, due to the failure of northern shallow instruments in 1975, measurements in the SAF above 2700 m are limited to three 1979 moorings. We make extensive comparisons with results from these studies and, where appropriate, with other current systems.

2. The observations

The four current meter moorings that make up the AUSSAF array were deployed near 50°30′S, 143°E during March 1993 and were recovered in January 1995. Figure 1 shows the location of the mooring array, with background shading of bathymetry (Smith and Sandwell 1994), as does Fig. 2 but at finer resolution. The white lines are surface dynamic heights relative to 2000 m, calculated from the Olbers et al. (1992) atlas. The array sits on the northern flank of the Southeast Indian Ridge, downstream of the point where the ridge, and the ACC,

turn southeastward, in approximately 3800 m of water. Maps of velocity variance from satellite altimetry (Morrow et al. 1994) show eddy energy is low upstream of the mooring site, but increases rapidly downstream beyond the turn in the ridge.

The moorings form the shape of a "T," oriented such that three moorings, called North, Central, and South, run in a line perpendicular to, and centered on the mean position of, the SAF, determined from climatology (Olbers et al. 1992). This main line, 70 km long, is coincident with World Ocean Climate Experiment (WOCE) hydrographic section SR3, from Tasmania to Antarctica, which was occupied six times between October 1991 and September 1996 (Rintoul and Bullister 1999; Rintoul and Sokolov 2000). The main line is also close to a high-density XBT line between Tasmania and Antarctica operated since 1991 and occupied 36 times (Rintoul et al. 1997). The fourth mooring, West, was placed 50 km upstream of the main line to allow for determination of alongstream gradients as well as crossstream. Figure 2 shows the position of each mooring and bathymetry at the full resolution available. Information available at the time of deployment indicated that the mooring site chosen was relatively flat, with depths between 3500 m and 3800 m; however, a seamount was found at the site that comes to within 2200 m of the sea surface and may affect the current flow.

In total eighteen Aanderaa current meters were de-

TABLE 1. Position, nominal depth, and dates of operation of each current meter. Where dates of operation are different for velocity and temperature, both are tabled. Also shown is the pressure level of the data after mooring motion correction (or mean pressure for the two deepest levels). Some gaps in data are filled by MM correction scheme; percentage of each record so filled is indicated.

Mooring	Latitude	Longitude	Nominal depth (m)	Pressure after MM correction (db)		Dates of observations (dd/mm/yy)	Dates after MM correction (dd/mm/yy)	Number of days simulated (%)
West	50°33.19′S	142°42.49′E	300	420	(T)	18/3/93–25/1/95	19/3/93–25/1/95	0
					(u, v)	11/5/93–28/7/93	19/3/93–28/7/93	40
West	50°33.19′S	142°42.49′E	600	780	(T)	18/3/93–25/1/95	19/3/93–25/1/95	0
					(u, v)	11/5/93–27/6/93	19/3/93–28/7/93	23
West	50°33.19′S	142°42.49′E	1000	1150		18/3/93–8/4/94	19/3/93–25/1/95	44
West	50°33.19′S	142°42.49′E	2000	2240		Instrument failed	19/3/93–25/1/95	100
West	50°33.19′S	142°42.49′E	3200	3320		18/3/93–20/4/94	18/3/93–20/4/94	0
North	50°24.95′S	143°31.97′E	1000	1150		19/3/93–30/4/94	19/3/93–30/4/94	0
North	50°24.95′S	143°31.97′E	2000	2240		19/3/93–13/12/94	19/3/93–30/4/94	0
North	50°24.95′S	143°31.97′E	3200	3320		Instrument failed	No simulation	0
Central	50°42.73′S	143°24.15′E	300	420		22/7/93–24/1/95	19/3/93–24/1/95	18
Central	50°42.73′S	143°24.15′E	600	780		18/3/93–21/7/93	19/3/93–24/1/95	81
Central	50°42.73′S	143°24.15′E	1000	1150		18/3/93–23/4/94	19/3/93–24/1/95	41
Central	50°42.73′S	143°24.15′E	2000	2240		18/3/93–24/1/95	19/3/93–24/1/95	0
Central	50°42.73′S	143°24.15′E	3200	3320		Instrument failed	No simulation	0
South	51°01.54′S	143°14.35′E	300	420		18/3/93–12/5/94	18/3/93–12/5/94	0
South	51°01.54′S	143°14.35′E	600	780		18/3/93–25/1/95	18/3/93–12/5/94	0
South	51°01.54′S	143°14.35′E	1000	1150	(T)	18/3/93–11/5/94	18/3/93–12/5/94	0
					(u, v)	18/3/93–11/5/94	18/3/93–12/5/94	28
South	51°01.54′S	143°14.35′E	2000	2240		18/3/93–28/5/94	18/3/93–12/5/94	0
South	51°01.54′S	143°14.35′E	3200	3320		18/3/93–4/5/94	18/3/93–4/5/94	0

ployed: five each on West, South, and Central; and three on North. The data return rate was approximately 60%. Five of the instruments ran for the full deployment period (23 months), three instruments returned no data at all, and the remainder returned records of varying length. Table 1 lists the position, nominal depth, and dates of operation of each instrument. All instruments measured temperature, current speed, and current direction. Instruments at 300 m and 3200 m on all moorings, and at 2000 m on Central, also measured pressure. Additional pressure gauges at 1000 m on all moorings suffered extreme sensor drift at different times during deployment, rendering useless most of these pressure records.

a. Removal of tides

As the focus of this study is mesoscale eddies, tides and other fluctuations with periods shorter than 40 h were removed from the velocity and temperature records. We used Thompson's (1983) "120i913" filter, which completely suppresses the seven principal tidal constituents, O_1, K_1, Q_1, P_1, M_2, N_2, and S_2, and the local inertial frequency. Signals of period 40 h and longer are passed through undisturbed.

b. Correction for mooring motion

Daily subsampled temperature and velocity records at nominal depths of 1000 m and above have been corrected for mooring motion using the method developed by Hogg (1986; 1991) and modified by Cronin et al. (1992). See appendix A for details.

Temperature and velocity from the instruments at 300, 600, and 1000 m on each mooring were corrected to constant pressure levels of 420, 780, and 1150 dbar, the mean pressures of these instruments averaged over the array. The West 2000-m instrument recorded no data, but the mooring motion correction software was used to simulate temperature and velocity at 2240 dbar. Data from the remaining deep instruments were left uncorrected; their mean pressures are 2240 and 3320 dbar.

Smaller gaps in the data have also been filled by the mooring motion correction scheme and Table 1 indicates what percentage of each record is filled. Where there was no data at the top two levels, we have not extrapolated from 1000 m because temperature gradients here are often too weak to give an accurate fit to the canonical temperature profile. This was the case on the North mooring for temperature and velocity and on the West mooring after day 149 for velocity only.

3. Temperature and velocity structure

In this section we first examine the mean temperature and horizontal velocity and then assess the variability in the records, including their vertical structure and coherence across the array. Vertical motion inferred from the current meter data completes the description of flow. We then explore the links between temperature and three-dimensional current velocity, particularly in relation to the position of a meander crest over the array,

TABLE 2. Mean and variance of temeprature and velocity for the full record length of each instrument. Velocity statistics are presented in both geographic and shear coordinates (see text for definitions).

Pressure (dbar)	Record length (days)		Mean					Variance				
			$\overline{T}$ (°C)	$\overline{u}$	$\overline{v}$	$\overline{\hat{u}}$	$\overline{\hat{v}}$	$\overline{T'^2}$ (°C)	$\overline{u'^2}$	$\overline{v'^2}$	$\overline{\hat{u}'^2}$	$\overline{\hat{v}'^2}$
	T	u,v		(cm s⁻¹) geographic		(cm s⁻¹) shear			(cm² s⁻²) geographic		(cm² s⁻²) shear	
West												
420	678	132	7.676	22.83	5.72	28.59	4.92	1.714	217.49	165.98	213.30	28.4
780	678	132	5.864	17.66	6.83	19.78	6.36	2.030	103.90	108.99	114.85	25.0
1150	678	337	3.878	11.86	1.62	16.46	4.45	0.609	75.58	185.84	69.02	44.8
2240	678	132	2.455	4.18	4.96	4.76	4.92	0.012	18.28	32.13	17.08	28.4
3320	399	396	1.324	1.42	−0.27	2.06	1.27	0.013	18.50	23.60	17.92	17.4
North												
1150	408	408	3.533	4.53	9.74	15.38	0.08	0.366	80.05	118.75	73.37	4.2
2240	408	408	2.282	1.50	3.31	4.24	0.03	0.014	6.68	11.59	9.26	4.1
Central												
420	677	677	7.339	19.01	13.97	31.01	0.54	1.751	216.20	420.47	220.67	12.5
780	677	677	5.273	15.50	11.06	24.51	−0.22	2.168	158.89	259.29	161.34	18.6
1150	677	677	3.589	11.57	5.53	16.40	−2.64	0.643	109.10	154.98	78.28	74.4
2240	678	678	2.376	3.32	2.92	5.26	0.54	0.009	14.79	21.55	15.58	12.4
South												
420	421	421	6.755	27.85	18.60	39.10	−1.96	1.591	366.34	353.06	291.02	17.8
780	421	421	4.762	21.24	12.83	29.57	−3.34	1.355	231.90	244.73	170.87	35.8
1150	421	421	3.267	16.07	7.57	20.75	−4.55	0.284	131.70	131.87	88.98	38.7
2240	421	421	2.157	5.43	2.36	7.11	−1.97	0.008	21.14	33.20	17.28	17.7
3320	421	421	1.152	0.37	2.14	2.66	0.77	0.009	14.62	37.56	25.23	24.0

as determined from satellite altimeter. We complete this section with a comparison of this site and the ACC sites previously monitored.

a. Mean temperature and velocity

The record-length mean velocities (Fig. 2) turn counterclockwise across the array. Strongest velocities correspond to shallowest instruments: 420 dbar on West, Central, and South, 1150 dbar on North. Record-length mean temperatures (Table 2) reveal the West mooring as the warmest on average, followed by Central, North, and then South, consistent with the direction of mean velocity recorded by the current meters. Velocity vectors at West (Fig. 2) are for their common record length of 132 days but also shown is velocity at 1150 dbar for its full 337 day record (dashed vector) for comparison with the other moorings. The Central mooring record length is 678 days; current vectors calculated for the first 421 days (record length of South) are not very different than shown: they are stronger by 2–3 cm s⁻¹ and 5°–6° more northward for the top three instruments with little change at depth. Mean current speeds are strongest at South: 33 cm s⁻¹ at 420 dbar compared with approximately 23 cm s⁻¹ at West and Central, decreasing to near 2 cm s⁻¹ at 3320 dbar on South and West.

Velocity vectors also turn about the vertical coordinate, rotating consistently anticlockwise with decreasing depth at South and Central, and clockwise at West. This has implications for the vertical velocity field, which we discuss in section 3b(3).

b. Variability of temperature and velocity

Time series of temperature and velocity show many similarities between moorings and, in the interest of conciseness, we illustrate the remainder of this work with examples from the South mooring only. Although South has only 420 days of observations, compared with 680 on Central, it is the most reliable mooring in that there are no gaps in temperature, and only at 1150 dbar were there small gaps in velocity, now filled by the mooring motion correction algorithm.

1) TEMPERATURE

Time series of temperature at five levels on the South mooring are shown in Fig. 3a, and in Fig. 3b temperature at 420 dbar on Central (thin line) provides information for the full deployment period. There is no evidence of seasonal variation, rather the behavior is episodic and the crossing of the SAF back and forth over the array is evident in the sharp temperature changes. A temperature section from CTD data along a segment of WOCE line SR3 during January 1994 (dates marked in Fig. 3) shows the clearly defined SAF near 51°S (Fig. 4). A cold core ring is evident to the north of the front near 48.5°S.

The beginning of the record is relatively cool with few large changes in temperature, suggesting south-of-front conditions. Near day 160, temperature rises sharply as the front moves over the array. Rapid shifts in temperature suggest that the front is within the array at

FIG. 4. CTD temperature (°C) section along part of WOCE SR3 during January 1994. Working current meters on the main line (solid circles) and CTD stations (dotted lines) are shown. The top 500 m is expanded.
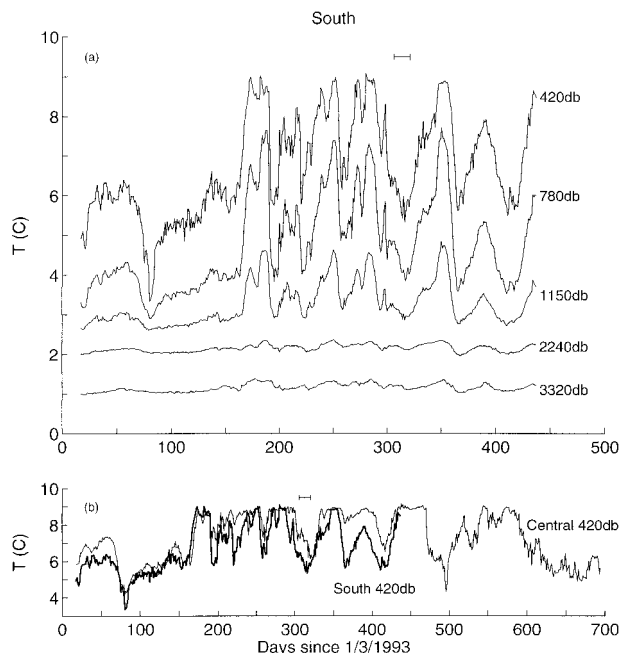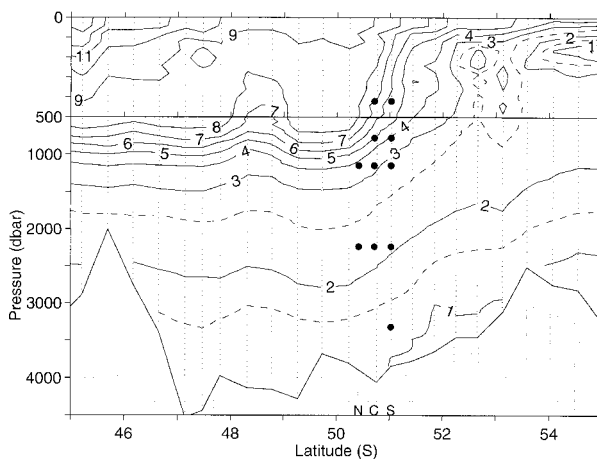
FIG. 3. (a) Time series of temperature from the South mooring, (b) time series of 420-dbar temperature from the Central mooring (fine line) and the South mooring (heavy line). Dates of CTD transect of Fig. 4 are marked by a line at 9.5°C.

this time until about day 320. Examination of four temperature sections from CTD measurements during the mooring deployment reveals that a change in temperature of 3°C at 420 dbar in the vicinity of the front would require a cross-frontal displacement of 80–180 km with an average of 114 km. As the temperature change is linear over that distance (from CTD data), the smaller changes of <2°C, which occur between days 160 and 320 correspond to displacements of <76 km, approximately equal to the distance across the array, confirming that the front is largely within the array during this time. Between days 320 and 470 the crossing of the front over the array becomes more periodic and lower in frequency, as the front moves consistently north or south over several weeks. Notice in the Central mooring record (Fig. 3b) that the maximum temperature (~9°C) is maintained for extended periods during this time (up to 40 days), suggesting that the front is mainly south of the array, and the moorings, particularly the northern ones, experience predominantly north-of-front conditions. The "plateau" near 9°C indicates the instrument is within the thick homogeneous layer of subantarctic mode water north of the front (Fig. 4; Rintoul and Bullister 1999). After day 470 temperature fluctuations of order 1°C occur on timescales of a couple of days, faster than previously seen in the record. Temperatures suggest the front is within the array until day 600 and thereafter they gradually reduce to south-of-front levels. The rapid temperature changes throughout most of these records indicate that for a significant por-

tion of the deployment period the SAF was within the mooring array; conditions south and north of the front were also sampled.

Temperature time series from all moorings are visually coherent throughout the water column and are significantly correlated in the vertical at a significance level of 95% ($C = 0.8$–0.97). Maximum correlation occurs at zero lag to within one day for all combinations of levels. Phase estimates for the frequency band 0.02–0.05 cpd, corresponding to a peak in spectral energy for both velocity and temperature [see section 3b(5)], indicate a slight tendency for shallow events to lead deep ones. The first empirical orthogonal function (EOF) of the vertical structure for temperature, whose shape is strongly baroclinic (Fig. 5), accounts for 97% of the variance on all moorings.

Correlation in the horizontal plane is also very high. Cross-correlations of temperature at the same level on different moorings show that neighboring moorings are significantly correlated at 95% for almost all levels. Only North and South are not significantly correlated, hinting that the distance across the array (~70 km) is roughly the same size as features crossing the array. Temperature along the main line is in phase to within one day at all levels and West leads the main line by approximately three days.

The integral timescale, τ_I, is defined as the integral of the autocorrelation function, $C(\tau)$, such that

$$\tau_I = \int_{j=-\infty}^{\infty} C(j\Delta t) \, \Delta t. \qquad (2)$$

Following Nowlin et al. (1985) we integrate over $j = \pm M$ where $M = 20\%$ of the number of observations, large compared with the lag number at which the autocorrelation function becomes statistically zero. The integral timescale for temperature is of order 20 days
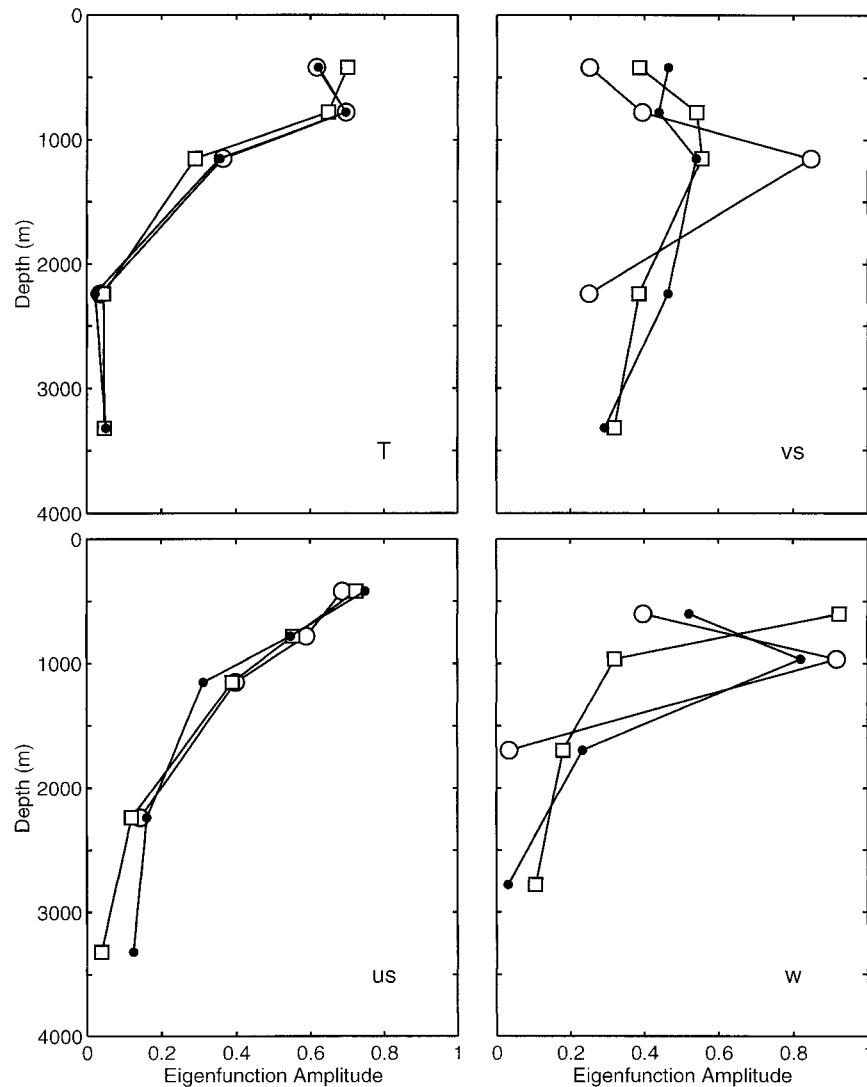
FIG. 5. First EOF for the vertical structure of temperature, alongstream velocity (us), cross-stream velocity (vs), and vertical velocity for the West (dots), South (squares), and Central (circles) moorings. For West, the common record length (132 days) is used.

at West and South, 30 at Central, and 70 at North. Most likely, τ_I increases equatorward because the SAF fully crosses the northern moorings less frequently than the southern ones. There is a small variation with depth but this has no consistent pattern and differs only 15% from the mean value.

Figure 6 gives an insight into the changing orientation of the front. At the beginning of the record, when the array is sampling the southern side of the front, temperatures at 1150 dbar are almost the same on each mooring giving no information as to front orientation. As the front moves southward over the array the difference between moorings becomes more distinct and front orientation can be inferred. For example, between days 80 and 170 the front moves across the array in such a way that West experiences a rapid increase in temperature while the others remain in south-of-front conditions, suggesting that the part of the front crossing the array has an orientation similar to the orientation of the main line, with current flow from south-southwest. Another example is of eastward flow near day 300 when temperature is warmest at the north mooring, gradually decreasing to coldest at South. Any mooring can experience the warmest temperature, including South (2% of record) but usually West (69%) or Central (18%), and flow directions vary from southwestward to northwestward through the eastern half of the compass.

2) Horizontal velocity

The observations of large-scale movement of the SAF from the temperature records lead us to question which
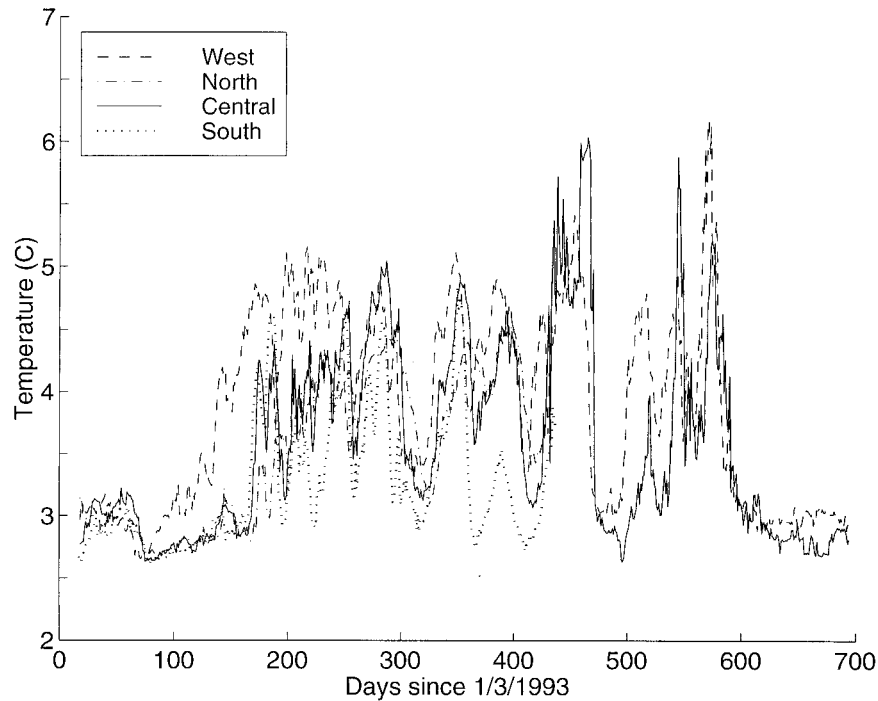
FIG. 6. Time series of temperature at 1150 dbar for all moorings.

reference frame is the most appropriate in which to consider the horizontal velocity. This question, common to the analysis of many current systems, is particularly important in the case of the ACC where the cross-stream heat and momentum fluxes are of direct relevance to climate. Not only is the definition of the cross-stream direction crucial, but the isolation of different frequency signals is also important for the calculation of eddy fluxes since many variations in the flow of the ACC are long-period meanders and lateral shifts of the front with dynamics distinct from higher-frequency eddy motions.

We present the velocity components relative to two frames of reference. The first is a geographic coordinate system such that alongstream is directed orthogonal to the main line of moorings, toward 104°T, which is the direction of mean ACC flow at this location (Olbers et al. 1992); cross-stream is along the main line, toward 14°T. While the ACC rarely follows this mean path, the value of this reference frame is that it allows our data to be more readily compared with the earlier ACC data (Bryden 1979; Sciremammano 1980; Bryden and Heath 1985), which were presented in a geographic coordinate frame. We refer to velocity components in geographic coordinates as eastward (u) and northward (v).

The second frame of reference is time-varying and was used by Hall (1986; 1989) in her analyses of the Gulf Stream and Kuroshio. Alongstream is defined as the daily direction of the vertical current shear, in our case between 420 and 2240 dbar ($[u_{420} - u_{2240}, v_{420} - v_{2240}]$), and cross-stream is 90° to the left of alongstream. The most compelling reason for choosing the direction

of vertical shear to define the alongstream coordinate is that it corresponds to the direction of the thermal wind, lying parallel to contours of dynamic height, and reliably approximates the direction of the baroclinic flow. The levels 420 and 2240 dbar were chosen because they span the depths where current shear and temperature changes are greatest; they also lead to time series of along- and cross-stream velocities with minimum variance. The shear definition allows the changing front orientation to be isolated from the true mesoscale eddy field, with most of the energy poured into the alongstream velocity component, leaving only small residuals in the cross-stream: the way one would intuitively expect the ACC to behave. Note that cross-stream velocities at 420 and 2240 dbar are identical due to the definition of the stream direction. We refer to velocity components in shear coordinates as alongstream ($\hat{u}$) and cross-stream ($\hat{v}$). Due to a lack of data at 420 dbar on North and at 420 and 2240 dbar on West after day 149, we define alongstream to be the direction of daily shear between 1150 and 2240 dbar on North and 1150 and 3320 dbar on West after day 149. Tests of these alternative definitions using South mooring data reveal that they reduce mean $\hat{u}$ by 3%–4% because less of the shear is captured in the narrower pressure range. This has little effect on the nature of $\hat{u}$ but time series of $\hat{v}$ are significantly altered. The variance of $\hat{u}$ and $\hat{v}$ increases by approximately 20%–30% compared with the 420–2240 dbar definition.

Consider first geographic coordinates. Figure 7 shows u and v for all instruments on the South mooring. There
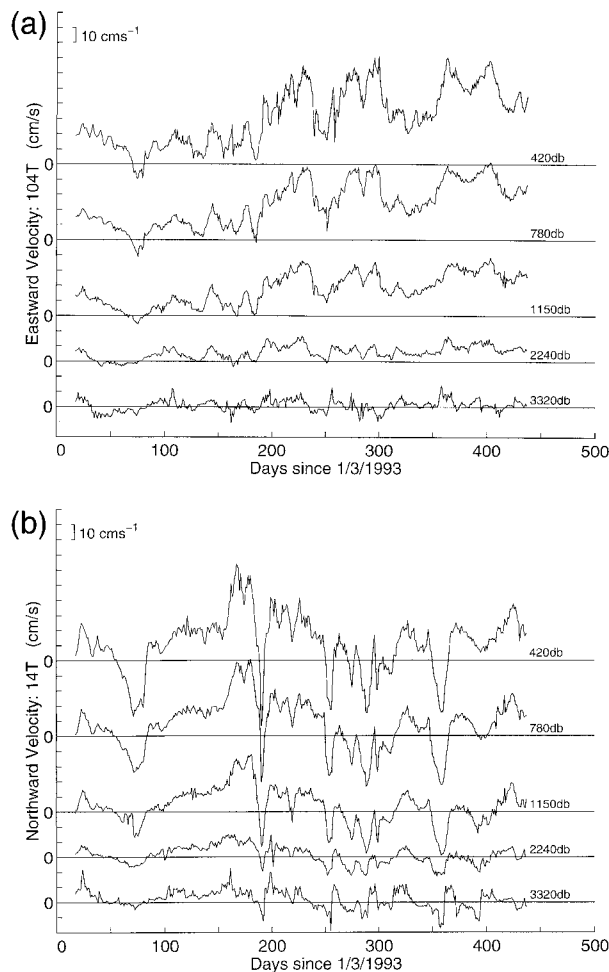
FIG. 7. Time series of velocity components in geographic coordinates for the South mooring: (a) eastward, directed toward 104°T and (b) northward, directed toward 14°T.
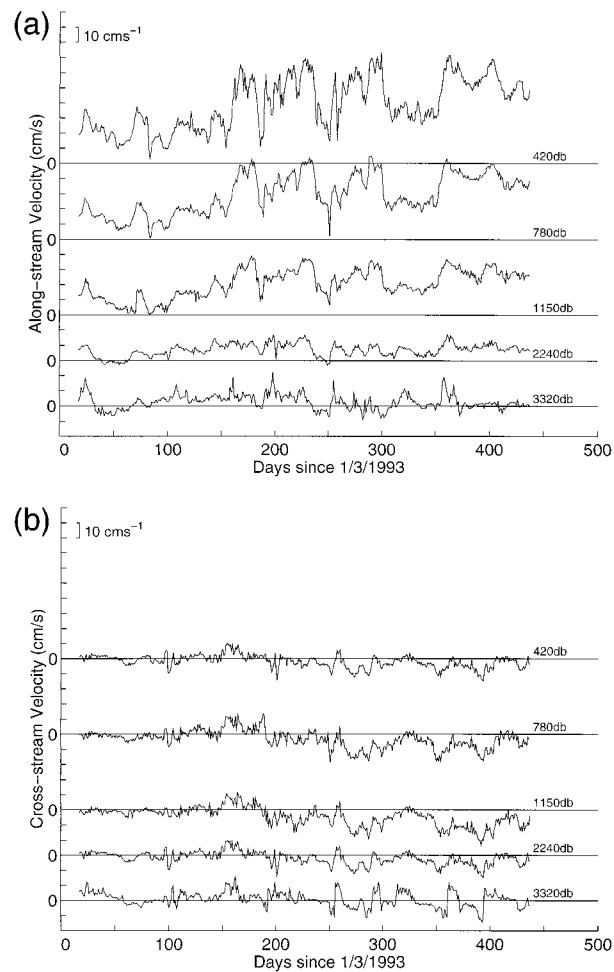
FIG. 8. Time series of velocity components in shear coordinates for the South mooring: (a) alongstream in the direction of 420–2240 dbar daily shear and (b) cross-stream, 90° left of alongstream.

is as much energy, often more, in the northward component of velocity as in the eastward, but on average, the flow is more eastward than northward. Vertical coherence is high for both components and current strength decreases gradually with increasing depth. Maximum current speed occurs on the South mooring and is 74 cm s^{-1} at 420 dbar.

In shear coordinates (Fig. 8) the alongstream velocity is (almost) always positive at 1150 dbar and above but deeper instruments record some upstream flow. Approximately one-third of the 3320 dbar record of $\hat{u}$ is upstream, suggesting a topographically induced reversal of flow at times when the shallower instruments record relatively low current speeds. The cross-stream component of velocity is up to an order of magnitude less than alongstream, as expected, and is predominantly negative (poleward) above 2240 dbar except between days 100 and 200. Vertical coherence is high for both components. Alongstream velocity gradually decreases with depth as for geographic coordinates, while cross-stream velocity is virtually depth independent, as it was found to be for the Gulf Stream (Hall 1986).

Mean alongstream velocity (Table 2) at each instrument is larger than mean eastward velocity at all depths, while mean cross-stream velocity is generally smaller than mean northward velocity, except at West where "eastward" coincides roughly with the direction of the mean current. The variance of the alongstream component remains as high as that for eastward velocity, while the cross-stream variance drops dramatically at the shallow instruments to only 10% of alongstream at 420 dbar. Both mean and variance of cross-stream velocity are nearly constant with depth although variance peaks slightly at 1150 dbar, more strongly at Central.

Like the temperature field, the velocity field shows no evidence of seasonal variation in either coordinate frame. Moreover, the episodic nature of flow at the moorings is more clearly displayed and is more obviously related to temperature when velocity is viewed in shear coordinates.

Integral timescales for velocity are difficult to interpret. Generally, τ_l is constant with depth to 2240 dbar and one of the components has a longer τ_l than the other. In geographic coordinates, at 2240 dbar and above, u has a τ_l of 40 days at South and 15 days elsewhere; v has a τ_l of 15 days at South, 25 days at West and Central, and 40 days at North. At 3200 m, τ_l is 5–10 days for both u and v, highlighting the different processes affecting these near-bottom instruments. In shear coordinates, τ_l for $\hat{u}$ is approximately 20–30 days above 2240 dbar, 15 days at 2240 dbar, and 7 days at 3320 dbar. For $\hat{v}$, τ_l increases with depth from 10 days at 420 dbar to 25 days at 1150 dbar, then decreases to 7 days below.

The visual vertical coherence of u, v, $\hat{u}$, and $\hat{v}$ is confirmed by calculations of cross-correlation coefficients: the top 4 instruments on each mooring are significantly correlated with a confidence level of 95% ($C = 0.71$–0.99). Velocity at 3320 dbar is significantly correlated with other levels for $\hat{v}$, but only with 2240 dbar for $\hat{u}$. Phase estimates (frequency band 0.02–0.05 cpd) indicate u, v, $\hat{u}$, and $\hat{v}$ are roughly in phase at 1150 dbar and above; below, deep events lead shallow by 10°–20° per 1000 m.

The first EOF of the vertical structure of along- and cross-stream velocity is shown in Fig. 5. The strongly baroclinic first EOF for $\hat{u}$ accounts for 94%, 96%, and 92% of the variance on West, Central, and South. North is not included due to lack of shallow data and EOFs on West are calculated for the common record length of 132 days. The first EOF for both u and v (not shown) have a similar shape to that for $\hat{u}$ and also account for close to 95% of the variance in the record. The first EOF for the vertical structure of $\hat{v}$ is quite different in shape and accounts for only 85% of the variance, with the remaining variance described principally by the second EOF (10%–15%). The shape of the first EOF for $\hat{v}$ is close to barotropic for West and South, but not so strongly as found for the Gulf Stream (Hall 1986); for Central the first EOF deviates sharply from barotropic at 1150 dbar as seen earlier in the variance figures (Table 2).

The pattern of correlation across the array for velocity in geographic coordinates is the same as that for temperature: significant correlation between all moorings except North and South. Surprisingly, moving to shear coordinates reduces the degree of spatial correlation. Only Central–South and Central–North remain significantly correlated for both $\hat{u}$ and $\hat{v}$, although there is some correlation of $\hat{v}$ for Central–West and West–South. This is a true reduction in the correlation coefficient, not an increase in the level of correlation required to achieve significance, r_c. In fact, for most of the correlations in shear coordinates, r_c is reduced because integral timescales are generally shorter and the number of degrees of freedom greater, making the test for significance less stringent.

The West mooring always leads the main line, for u,

v, and $\hat{u}$, and the South mooring always leads Central, which leads North, so that features propagate through the array, roughly speaking, from west to east. Correlations between $\hat{v}$ on different moorings are weak, and we cannot infer anything from these about the lag of maximum correlation. Typically the time lag from South to Central (35 km) and Central to North (35 km) is approximately 2 days. The West mooring leads Central by approximately 3 days for u and 5 days for v and $\hat{u}$. The shortest distance from West to Central is 52 km and the most appropriate time lag to apply to this distance in calculating propagation speed is that for eastward velocity (u), along 104°T. Thus, on average, eddies propagate through the array at 20 cm s^{-1} toward 59°T. Bryden and Heath (1985) reported that energetic eddies southeast of New Zealand propagate southeastward at about 12 cm s^{-1}, nearly twice as slow as south of Australia.

We believe that the shear coordinate frame is the most appropriate for considering the motion of the SAF, primarily because the front is so mobile and a coordinate frame that moves with the current is better able to separate the flow of the stream from the changing orientation of the front. It also enables the link between the strength of flow and other properties to be seen more clearly. Finally, it greatly improves the statistical significance and coherence between moorings and with depth of cross-stream eddy fluxes (section 4). We will therefore, henceforth, focus on velocity in shear coordinates, retaining geographic coordinate velocities for comparison with other studies.

3) VERTICAL VELOCITY

In order to complete the picture of the velocity field we have calculated vertical velocity, w, from the current meter data using a modification of methods described in earlier studies (Bryden 1980; Hall 1986; Lindstrom and Watts 1994). See appendix B for details. We have no independent measurements of w with which to verify w inferred from the current meter data. However, Lindstrom and Watts (1994) have shown that vertical motion inferred from current meter measurements agrees closely with directly observed vertical motion from RAFOS float pressures on isopycnal surfaces and, for timescales longer than 16 days, also agrees well with vertical motion calculated from the quasigeostophic vorticity equation using inverted echo sounder measurements.

Figure 9 shows time series of vertical velocity on the South mooring at four pressure levels: 600, 965, 1695, and 2780 dbar, the midpoints between adjacent instruments. The velocities have been smoothed with a 5-day running mean; positive w indicates upwelling. Vertical velocity is strongest above 1150 dbar and decreases quickly below. Typical values for w are of order 1 mm s^{-1} with peaks up to 5 mm s^{-1}—the same order of magnitude as found for the Gulf Stream (Hall 1986; Lindstrom and Watts 1994) and Kuroshio (Hall 1991). Ver-
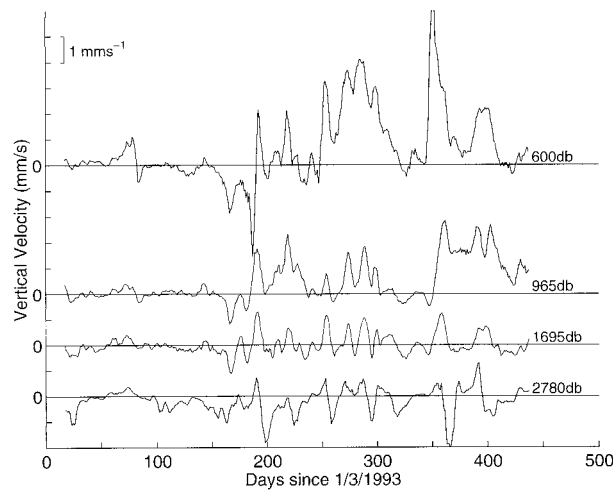
FIG. 9. Vertical velocity between adjacent instruments on the South mooring. Pressure shown is halfway between instrument pairs.

tical coherence is high for all moorings with significant correlation (95%) between the top three levels, which are in phase to within one-day. There is good agreement between South and Central with South leading by 4 days. Vertical motion on the West mooring (not shown) shares some gross similarities with that on South for the first 149 days in that there is weak upwelling followed by stronger downwelling. The downwelling event on West, thought it begins a month earlier than it does on South, is much stronger and more persistent. We ignore the North mooring as w is only available at 1695 dbar where vertical motion is small.

Recall the rotation with depth of the mean horizontal velocity vectors in Fig. 2. At the South and Central moorings, the sense of rotation is clearly anticyclonic with decreasing depth (veering). Following Bryden (1980), in the mean we would expect to see upwelling at South and Central, which is confirmed in Table 3. The North mooring exhibits little rotation and consequently experiences very weak vertical motion. Rotation of mean velocity vectors at West is cyclonic for the short shallow records, indicating downwelling, and weakly anticyclonic for the full records at 1150 and 3320 dbar, indicating upwelling as for South and Central.

Integral timescales for vertical velocity are approximately 20 days above 1150 dbar and 6 days below. There is also good vertical correlation between the top

three records of w, significant at 95%, and maximum correlation occurs at zero lag.

The first EOF for the vertical structure of w (Fig. 5) accounts for approximately 90% of the variance, has no zero crossing, and looks like the vertical structure associated with the first baroclinic mode. Eigenfunction amplitude decreases monotonically from a maximum at the shallowest instrument on the South mooring, while the Central and West moorings have a maximum at 1150 dbar. The vertical structure of vertical motion in the Gulf Stream is very similar with strong vertical coherence, 82% of the variance accounted for by the first EOF, no zero crossing, and a thermocline maximum in eigenfunction amplitude (Hall 1986). The Kuroshio Extension, in contrast, showed poor vertical coherence and had only 58% of the variance in the vertical structure accounted for by the first EOF, the second accounted for a further 29% (Hall 1991).

4) THE LINK BETWEEN T, $\hat{u}$, $\hat{v}$, AND w

To examine the link between temperature, velocity, and rotation of current vectors with depth, we combine time series of temperature, along- and cross-stream velocity at 420 dbar, vertical velocity at 600 dbar, and current direction at 420 and 780 dbar from the South mooring (Fig. 10).

In section 3b(1) we identified different periods in the temperature time series, which were characterized by different timescales of variability and which we believe corresponded to different positions relative to the front. These periods are also mirrored in the alongstream velocity: for days 0–160 low to moderate current speed and little high-frequency variability; for 160–320 high speeds and rapid variation; for 320–470 high and moderate speeds varying in a periodic manner; for 470–600 (not shown in Fig. 10) rapid changes between high and low speed; and for 600–700 (not shown) low speed and declining high-frequency variability. Here we consider low speed to be <30 cm s^{-1}, moderate 30–50 cm s^{-1}, and high >50 cm s^{-1}. Alongstream velocity is strongest when temperature at 420 dbar is close to 8°C and drops off sharply when temperature rises or falls away from this value. A temperature of 8°C at 420 dbar, then, seems to be a good indicator of the core of the SAF, agreeing well with Belkin's (1990) definition: the location where

TABLE 3. Mean and rms vertical velocity (mm s^{-1}) between adjacent instruments. Pressure at instrument and midway between instrument pairs is shown.

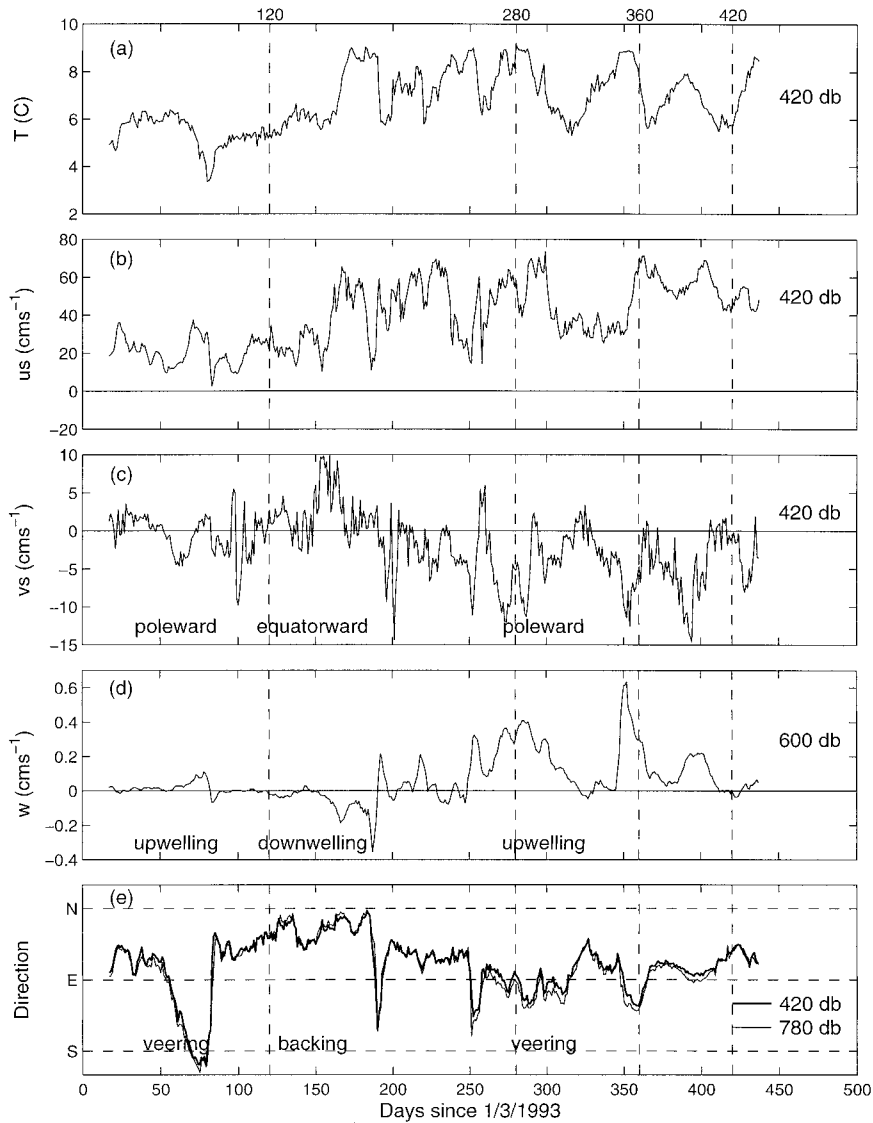| Pressure (dbar)	Midpoint (dbar)	West $\overline{w}$	West w_{rms}	North $\overline{w}$	North w_{rms}	Central $\overline{w}$	Central w_{rms}	South $\overline{w}$	South w_{rms}
420									
780	600	−0.59	0.85	—	—	0.38	0.89	0.64	1.51
1150	965	−0.93	1.31	—	—	0.85	1.93	0.48	0.92
2240	1695	−0.12	0.46	0.01	0.20	−0.23	0.44	0.01	0.39
3320	2780	−0.01	0.16	—	—	—	—	−0.20	0.52

FIG. 10. Time series from South showing the link between rotation of current vectors with depth, cross-stream, and vertical velocities: (a) temperature, (b) alongstream velocity, and (c) cross-stream velocity, all at 420 dbar, (d) vertical velocity at 600 dbar, and (e) current direction at both 420 and 780 dbar. Downwelling (upwelling) and cold (warm) advection occur when the current is backing (veering). The four days highlighted relate to Fig. 11.

the temperature gradient at 300 m is strongest and temperature is between 3° and 8°C.

Cross-stream velocity is much weaker and more erratic than alongstream (scale of $\hat{v}$ is expanded to four times that for $\hat{u}$ in Fig. 10). Its variation is not random, though as there are extended periods of poleward and equatorward flow, particularly after day 200.

Cross-correlations between $\hat{v}$ and T are negative and are significant at 95% or higher for all levels at South and at 90% or higher for 5 of the 11 remaining instruments, suggesting strong poleward transport of heat by eddy fluxes. This is a vast improvement on the correlations between v and T where only instruments at or deeper than 2240 dbar showed any significant correla-

tion. Cross-correlations between $\hat{u}$ and T are only significant at Central and South and only above 1150 dbar. The correlation coefficients themselves can be as large as those for $\hat{v}$ and T but, because the integral timescales are generally longer for $\hat{u}$, significance is not achieved. Cross-correlations between w and $\hat{v}$ show anticorrelation at 95% significance; there is also a significant positive correlation between w and $\hat{u}$.

The bottom panel of Fig. 10 shows that direction at 420 dbar (heavy line) and at 780 dbar (fine line) are close and the small deviation gives the rotation of the horizontal velocity vectors with depth. When the fine line is below the heavy line, the current is veering, which is an anticyclonic rotation of the horizontal velocity
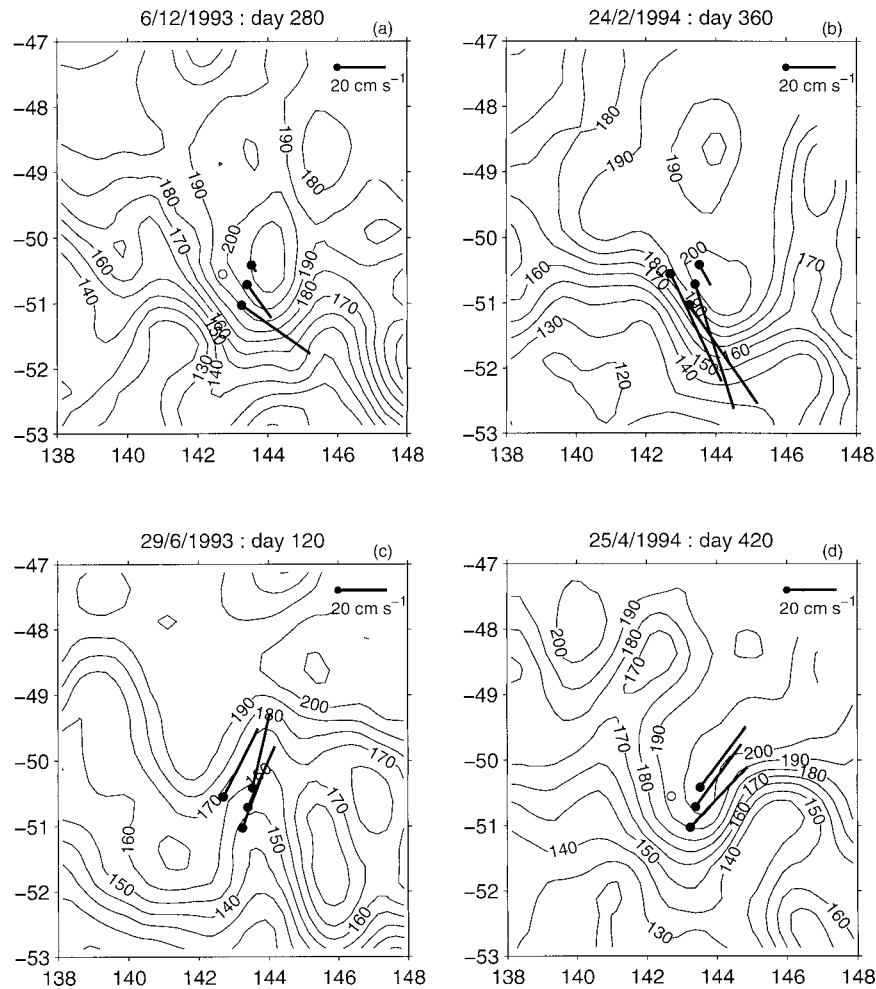
FIG. 11. Ten-day average current vectors at 1150 dbar on four days, and corresponding sea surface height. Sea surface height anomalies from the TOPEX/Poseidon, *ERS-1*, and *ERS-2* satellite altimeters, merged and mapped onto a 0.25°grid [the CLS "MSLA" dataset (Le Traon et al. 1998)], have been added to the 0–2000-m dynamic height from the Olbers et al. (1992) climatology.

vectors with decreasing depth. Equation (B3) says that veering of a current is associated with upwelling and Fig. 10 shows how closely time series of w and turning of the current correspond. The opposite scenario, backing, is associated with downwelling.

The velocity and temperature records, both in the mean (Fig. 2 and Table 2) and in the time series (only shown for South), provide evidence of a meander over the array, its presence in the mean fields suggesting that it persists for extended periods. The meander is sometimes west of, directly over, or east of the array and could be either several meanders propagating through, or one quasi-stationary meander shifting small distances, perhaps responding to variations in the strength of the current flow. We use satellite sea surface height (SSH) measurements to provide independent evidence of meander location. Annual-mean dynamic height of the sea surface relative to 2000 dbar from Olbers et al. (1992) has been added to surface height anomalies from

the CLS "MSLA" dataset (Le Traon et al. 1998) to provide a sequence of SSH maps at 10-day intervals from October 1992 to the present.

The SSH maps corresponding to the deployment period of the moorings show that the meanders do indeed propagate eastward through the array but can become stalled. The time for half a meander to propagate through the array varies from 10 to 90 days. The stalling may be due to obstruction of the flow by the seamount at the array, or the meander could be the crest of a quasi-stationary Rossby wave that is occasionally pushed through the array by an increase in current flow. The distance between the meander and one downstream, about 500 km (e.g., Fig. 11c), is close to the wavelength that a quasi-stationary Rossby wave would have at 50°S in an eastward flow of 10 cm s^{-1} (=520 km) (Pedlosky 1987). There is no clear connection between the meander's stationarity and current speed at the array.

Lindstrom et al. (1997) have studied the relationship

between vertical motion and the phase of meanders in the Gulf Stream and found that backing, cold advection, and downwelling, ''bcd'' to use Lindstrom et al.'s mnemonic, occur entering a trough. Veering, warm advection, and upwelling (''uvw'') occur exiting a trough. If this relationship is applicable outside the Gulf Stream, then we would expect our observations to reveal veering, warm advection and upwelling (backing, cold advection, and downwelling) entering (exiting) our Southern Hemisphere meander crest. We define a crest to be the maximum in anticyclonic curvature of a meander, which is the meander's most poleward excursion in a zonal flow, consistent with the usual Northern Hemisphere convention.

From the SSH maps, the location of meanders relative to the moorings can be clearly seen. Whenever the western edge of a meander crest was over the array, the moorings revealed veering, warm advection and upwelling. The backing scenario was observed when an eastern edge was over the array. To illustrate we give two examples of each scenario: case A, array on western edge of crest; and case B, array on eastern edge.

Figures 11a,b show SSH for case A (days 280 and 360) with current vectors from the 1150 dbar current meters overlaid (the level with fewest gaps). The current vectors are closely aligned with the surface height contours. Referring to Fig. 10, we see that there is strong upwelling on both days (2–3 mm s^{-1}) at the South mooring, the current is veering, and cross-stream flow is poleward, producing warm advection. For case B (days 120 and 420, Figs. 11c,d), the current is backing, vertical motion is weakly downward, and cross-stream flow is either weakly equatorward (cold advection) or zero.

Thus, the relationship between vertical motion and meander phase described by Lindstrom et al. (1997) for the Gulf Stream also holds for the SAF and probably the ACC in general.

Before this section is complete there is an apparent paradox that must be examined. While the results of this section support the results of Lindstrom et al. (1997), the story told by the mean velocity vectors of Fig. 2 appears not to. The curving of horizontal velocity vectors across the array suggests that in the mean the array is on the eastern edge of the meander crest and is experiencing flow exiting the crest. But, the rotation of horizontal velocity with depth indicates mean vertical motion is upward at Central and South, when we expect downward vertical motion in flow exiting an ACC meander crest. The simple explanation is that we cannot make assumptions about the location of the meander crest in relation to the mooring array relying only on the direction of current flow at the array. The SAF is obviously a very mobile feature and not only changes its orientation in the form of meanders but the meanders themselves change their orientation relative to geographic coordinates as they grow and steepen, a behavior widely documented for the Gulf Stream (e.g., Lindstrom et al. 1997). Time series of direction in Fig. 10

TABLE 4. Comparison of characteristic timescale and amplitude of fluctuations, vertical shear, and vertical temperature gradient at AUSSAF, southeast of New Zealand, and in northern and central Drake Passage.

	AUSSAF	N.Z.[a]	Drake (N)	Drake (C)	Units
Timescale	20	20	5–10[b]	10[b]	days
			12–15[c]	20–50[c]	
Amplitude	30	20	20[d]	20[b]	cm s^{-1}
	1000 m	1000 m	2700 m	1000 m	
$\overline{u_z} \times 10^2$					
~1000 m	1.0	0.4	2.0[e]	0.3[d]	cm s^{-1} m^{-1}
>2000 m	0.5	0.03	0.6	?	
$\overline{\theta_z} \times 10^2$					
~1000 m	0.2	0.2	0.1[f]	0.06[g]	°C m^{-1}
>2000 m	0.07	0.07	0.06[f]	0.07[g]	

[a] Bryden and Heath (1985)—2-yr CMs.
[b] Bryden (1979)—FDRAKE 1975, 1-yr CMs.
[c] Inoue (1985)—DRAKE 1979, 1-yr CMs.
[d] Pillsbury et al. (1979)—FDRAKE 1975.
[e] Whitworth et al. (1982)—FDRAKE 1975 + CTDs.
[f] Nowlin and Clifford (1982)—1975–80 CTDs.
[g] Johnson and Bryden (1989)—FDRAKE 1975 + 1977 Drake Cluster array.

show that there is no one flow direction more predisposed to veering and upwelling than any other, although, curiously, backing and downwelling seem only to occur when flow is northeastward (in this 2-yr record).

5) COMPARISON OF TEMPERATURE AND VELOCITY AT OTHER ACC SITES

The three SAF sites monitored to date all experience strong deep flow with temperature and velocity highly vertically correlated and virtually in phase at all levels. Small lags show that, at all sites, deep velocity events lead shallow and shallow temperature events lead deep. Table 4 lists characteristic features of the velocity and temperature fields for the three SAF sites and for central Drake Passage, the most studied location in the ACC.

Integral timescales [as calculated in section 3b(1)] are given for each of the four sites (line 1 of Table 4), showing that timescales at AUSSAF and southeast of New Zealand are similar and are longer than at both Drake Passage sites. A second calculation of timescales in Drake Passage (line 2 of Table 4) was made by Inoue (1985) using a different method. His timescales are longer than the integral timescales of Bryden (1979) but confirm that the northern passage varies more rapidly than the central and southern passage.

The characteristic amplitude of fluctuations near 1000 m is larger at AUSSAF than that southeast of New Zealand or in central Drake Passage. We were unable to find a reference reporting the amplitude near 1000 m in northern Drake Passage, but note that at 2700 m fluctuations there frequently reach 20 cm s^{-1}. We therefore expect that fluctuations near 1000 m in northern Drake Passage would be at least as large as those at AUSSAF.
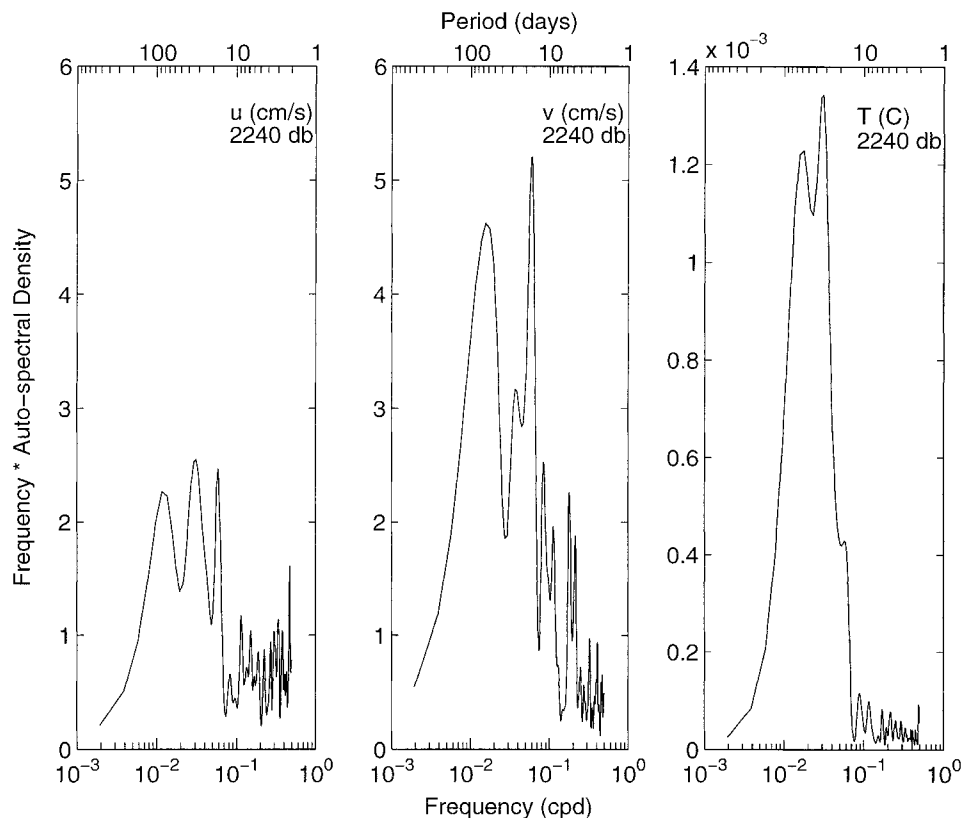
FIG. 12. Autospectra of along- and cross-stream velocity and temperature at 2240 dbar on the South mooring.

Average vertical current shear at AUSSAF and in northern Drake Passage are very similar, while that southeast of New Zealand and in central Drake Passage are a factor of 2–3 less than at AUSSAF near 1000 m and an order of magnitude less below 2000 m (for New Zealand). The depth guides given for the two estimates are approximate since different measurement levels were used in each study.

The vertical temperature gradient below 2000 m is the same for all sites. Near 1000 m, the three SAF sites have similar temperature gradients. In central Drake Passage, the temperature gradient near 1000 m is as small as that below 2000 m.

Autospectra of T, u, and v (geographic coordinates) south of Australia at 2240 dbar are shown in Fig. 12. Spectral energy is high in the broad band from 20 to 120 days for all of T, u, and v, and v also has energy in the 5–15 day band. Southeast of New Zealand, spectra are similar, but for u there was little energy at periods less than 80 days. In contrast, Drake Passage spectra for u and v show most energy is concentrated in the band 10–50 days, for the central passage (Bryden 1979).

In summary, conditions at the AUSSAF array and in northern Drake Passage are almost identical, although timescales in northern Drake Passage are shorter than at AUSSAF. Conditions southeast of New Zealand are similar in many respects to those at AUSSAF—timescales, vertical temperature gradient, and spectra—but the characteristic amplitude of fluctuations is one-third less and the vertical velocity shear is also considerably less than at AUSSAF. Central Drake Passage is very different to the three SAF sites, experiencing a weaker flow regime with smaller amplitude fluctuations, weaker shear, and weaker temperature gradients.

4. Eddy fluxes across the SAF

The two objectives of this section are to 1) present the best estimate of cross-ACC eddy fluxes for the AUS-SAF array and 2) compare AUSSAF eddy fluxes with those at other ACC locations. To achieve the first, we need to isolate the "eddy" band, which is thought to play such a crucial role in the transfer of properties across the ACC fronts, from the "low-frequency" band composed of meanders, rings, and large-scale shifts of the front, which are dynamically very different. We also need to choose a coordinate frame whose alongstream component best represents the alongstream flow of the ACC.
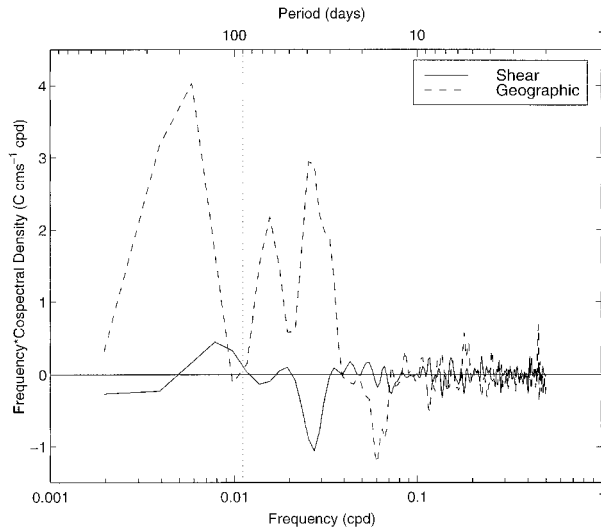
FIG. 13. Cospectra of cross-stream velocity and temperature, and northward velocity and temperature, at 420 dbar on the South mooring. The dotted line marks a period of 90 days.

a. Frequency bands and coordinate frames

Nowlin et al. (1985), examining cospectra of fluctuation temperature and cross-stream velocity, found that periods between 40 h and 90 days accounted for the eddy signal in Drake Passage. Similar variance-preserving cospectra in both geographic ($v \times T$) and shear ($\hat{v} \times T$) coordinates are shown in Fig. 13 for the South mooring at 420 dbar. The cospectrum in shear coordinates suggests 90 days is also, coincidentally or not, a good cutoff for the AUSSAF data, neatly separating poleward fluxes at periods less than 90 days from an equatorward peak at longer periods. The poleward eddy fluxes at all levels at South are concentrated in the band 30–80 days; at West and Central, poleward peaks extend to higher frequency (~20 days). In geographic coordinates (Fig. 13), heat fluxes are equatorward for all periods longer than 30 days as varying front orientation dominates the eddy signal. Nevertheless, 90 days is an obvious separation between eddy and low-frequency motions in this coordinate frame also. We therefore define eddies to be all motions with periods 40 h to 90 days. The fluxes brought about by these eddy motions are our primary interest, but we also examine fluxes by motions with periods longer than 90 days (low-frequency) and fluxes by eddy and low-frequency motions combined (all-frequency).

The shear coordinate frame, which so clearly described the horizontal velocity field, not surprisingly also gives the best flux estimates. We calculated fluxes in two other coordinate frames: geographic [see section 3b(2)] and 90-day (as used by Nowlin et al. 1985), where alongstream is in the direction of the time-varying 90-day low-passed current. We found that fluxes in any frame other than shear are not coherent between moorings or with depth and are generally not statistically significant (Table 5). We, therefore, consider the best estimate of cross-stream eddy fluxes for the AUSSAF array to be those calculated from bandpassed data in shear coordinates and averaged over the array (excluding short records at West).

Our second objective, comparison with other ACC eddy fluxes, is problematic due to the various definitions of alongstream. It would seem preferable to compare two sites with fluxes calculated using the same method. Then, fluxes from southeast of New Zealand would be compared with our geographic coordinate, all-frequency fluxes, and the Nowlin et al. Drake Passage fluxes with our 90-day coordinate, bandpassed fluxes. In practice, though, we have seen that only the daily varying shear coordinate frame produces coherent, statistically significant cross-stream fluxes at our array, which may reflect more active meandering of the SAF at the AUSSAF site. We argue, therefore, that nothing is gained from degrading our flux estimates by using the same coordinate frame as that used at another site in order to compare like with like. Only shear coordinate fluxes have any meaning at the AUSSAF site, and we therefore only use these when comparing with fluxes from other sites. For the remainder of this section, then, we omit reference to coordinate frame, it being understood that only fluxes in shear coordinates are presented.

We note in passing that eddy flux estimates in Drake Passage and southeast of New Zealand would also benefit from the shear coordinate frame. The success of the 90-day coordinate frame in Drake Passage was primarily so for the central passage where flow is principally through passage, turning sharply northward as the ridge extending from Elephant Island is encountered (Pillsbury et al. 1979). Indeed, Bryden and Pillsbury (1977) found that the direction of mean velocity shear in the

TABLE 5. Cross-stream eddy heat flux, $\rho_o C_p \overline{v'T'}$ in two frequency bands and three coordinate frames at the South mooring. Significant correlation at 90% confidence level is indicated by † and at 95% by ‡.

Pressure (dbar)	All-frequency (kW m^{-2})			Bandpassed (kW m^{-2})		
	Geographic	Shear	90-Day	Geographic	Shear	90-Day
420	165.63	‡−91.89	31.37	−11.08	‡−44.96	2.33
780	7.75	−98.47	−36.08	−33.80	‡−35.16	−13.57
1150	−25.33	−41.20	−23.90	−20.72	‡−18.64	−8.78
2240	†−8.21	‡−5.53	‡−6.92	‡−5.08	‡−3.32	‡−3.75
3320	‡−10.43	‡−7.73	‡−9.76	‡−6.74	‡−5.56	‡−6.31

central passage during 1975 was within 5° of the through-passage direction. In the northern passage, however, in the vicinity of the SAF, flow direction and current speed are highly variable (Pillsbury et al. 1979— their Fig. 8, mooring 2) and eddy heat flux calculated using the 90-day coordinate frame may not be representative of the true cross-stream heat flux. Southeast of New Zealand, the flow direction is also highly variable. Bryden and Heath (1985) show salinity contours at 200 m and current direction in April and November 1978. In April the flow is primarily northward, reversing in November to be toward the southwest. The geographic coordinate frame used by them does not represent the time-varying direction of the stream, and it is not surprising that eddy heat fluxes calculated for this array are not statistically significant.

Particularly in the case of eddy momentum flux, we are interested in the direction of the fluxes relative to the core of the SAF, rather than relative to the array location, to determine whether the Reynolds stresses act to decelerate or accelerate the mean flow. In order to isolate conditions on the north and south sides of the current, we have taken a very simple approach and used temperature at 1150 dbar as the criterion. Based on time series of temperature from the AUSSAF current meters and from examining six repeats of WOCE hydrographic transect SR3, we have chosen $T_{1150} > 4°C$ to represent the north side of the front and $T_{1150} < 3°C$ the south side. Fluxes for the north side of the front are calculated using data at all times where the criterion for north side conditions is satisfied, and similarly for fluxes on the south side.

b. Heat flux

Cross-stream eddy heat flux is calculated as $\rho_o C_p \hat{v}'_i T'_i$, where $\hat{v}'_i$ and T'_i are fluctuation cross-stream velocity and temperature at time t_i, ρ_o is a representative water density for the location ($=1035$ kg m^{-3}), and C_p is the specific heat at constant pressure (≈ 4000 J kg^{-1} °C^{-1}).

Time series of cross-stream heat flux are shown in Fig. 14 for the top three levels on the South mooring for the eddy and low-frequency bands. Note the change of scale for the 1150-dbar fluxes. Black lines above the curve identify times when the array experiences north-of-front conditions, black lines below indicate times of south-of-front conditions. Fluxes for the two deep instruments (not shown) have similar features to the shallow fluxes but are an order of magnitude smaller.

Low-frequency heat fluxes are statistically significant only at the Central mooring due to its longer record length. For all moorings, though, time series show that the majority of low-frequency events are poleward, produce heat fluxes that can be as large as those by eddies, and are sustained over periods of weeks rather than days.

As noted in section 3, there is a quiet time recorded at the start and end of our observations: the first 140 days and days 610–700 (at Central), corresponding to
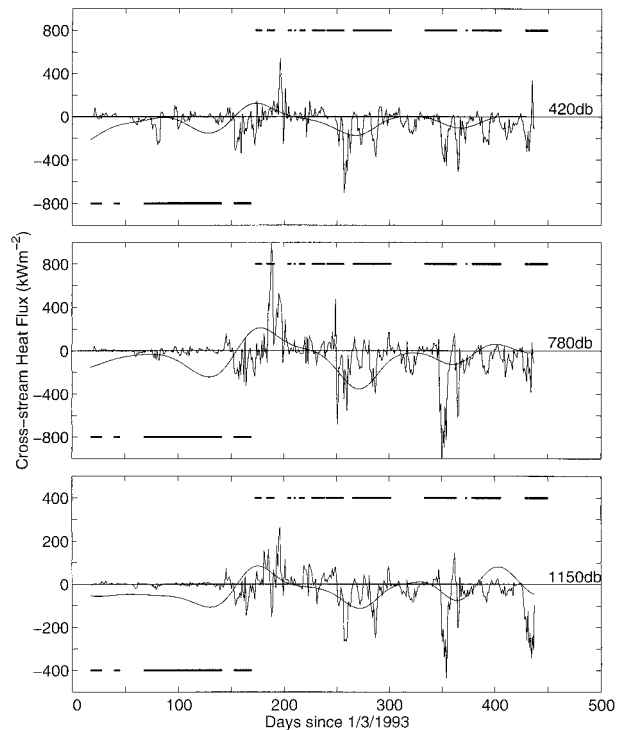

FIG. 14. Time series of cross-stream eddy heat flux $\rho_o C_p \hat{v}' T'$ (shear coordinates) for the top 3 instruments on the South mooring. The eddy band (40 h–90 days) and low-frequency band (>90 days) are superimposed. Times when the array is on the northern/southern side of the front are marked above/below the curves.

south-of-front conditions. This shows up in the heat fluxes as very small eddy fluxes and small but growing low-frequency fluxes. Also, at these times the eddy fluxes are largest at 420 dbar and decrease with depth. When the array is in the core of, or north of, the front, eddy fluxes are usually largest at 780 dbar and fluxes at all depths are larger than at times of south-of-front conditions. Low-frequency fluxes are usually largest at 780 dbar, regardless of position relative to the front. Both eddy and low-frequency fluxes are coherent with depth and between moorings.

The record-length mean heat fluxes for bandpassed data (Fig. 15a) show a highly consistent picture of poleward heat flux. Eight of the 16 flux estimates are significantly different from zero at 95% and a further 2 estimates are significant at 90%. The average of these four profiles, the best estimate of cross-stream eddy heat flux at the AUSSAF array (Table 6 and Fig. 15b, solid circles) shows poleward eddy heat flux at all levels, with a depth-average of 11.3 kW m^{-2}.

Figure 15b shows profiles of cross-stream all-frequency heat flux for southeast of New Zealand (open triangles) and northern Drake Passage (open squares), both in geographic coordinates, which may be compared directly with the AUSSAF all-frequency fluxes (open circles). Eddy band fluxes across the 90-day low-passed current in northern Drake Passage (solid squares) may
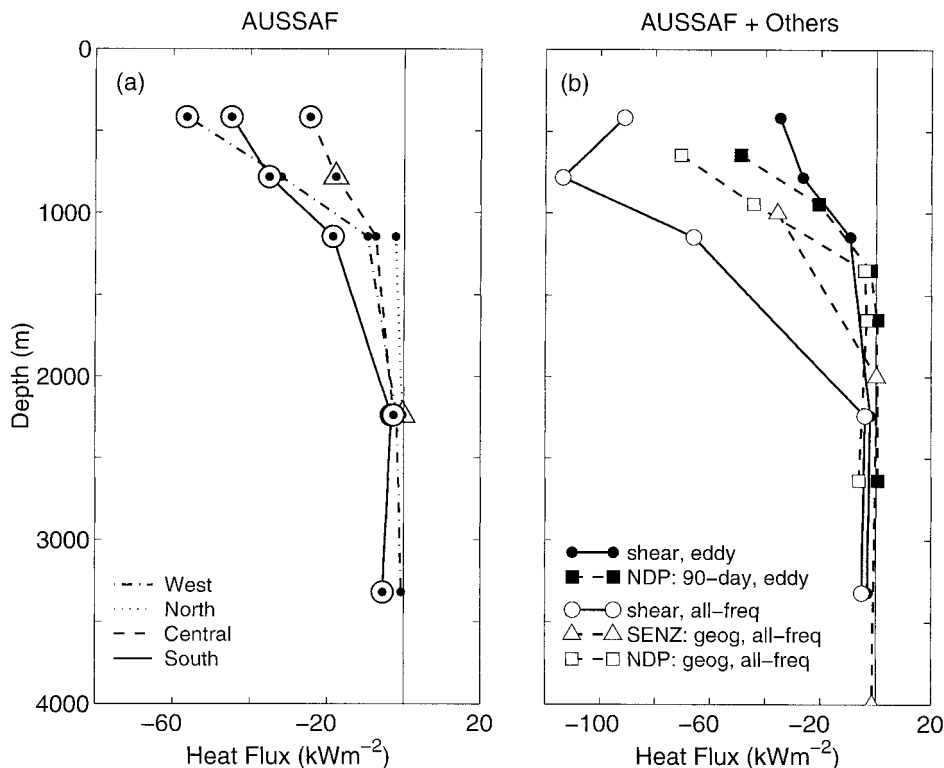
FIG. 15. Profiles of cross-stream eddy heat flux $\rho_o C_p \overline{v'T'}$. (a) Four AUSSAF moorings, shear coordinate, bandpassed data. Symbols over the data point indicating statistical significance are triangle = 90% and circle = 95%. (b) Representative profiles from all available SAF sites: best estimate from AUSSAF moorings—array-mean of shear-coordinate, bandpassed fluxes; array-mean of AUSSAF shear-coordinate, all-frequency fluxes; southeast of New Zealand (Bryden and Heath 1985); and two northern Drake Passage estimates (Nowlin et al. 1985).

be directly compared with AUSSAF eddy fluxes (solid circles). All fluxes are poleward except below 1500 m in northern Drake Passage, where they are not statistically significant. Near 1000 m, AUSSAF all-frequency heat fluxes are twice as large as fluxes southeast of New Zealand and in northern Drake Passage, while eddy heat fluxes in northern Drake Passage and at AUSSAF are approximately the same size, indicating that low-frequency motions are more active at the AUSSAF array. Near 2500 m, AUSSAF all-frequency fluxes are the same size as those in Drake Passage and an order of magnitude larger than those southeast of New Zealand.

TABLE 6. Best estimate of profiles of eddy heat and momentum fluxes at the AUSSAF array (shear coordinate, bandpassed data).

Pressure (dbar)	Eddy heat flux $\rho_o C_p \overline{v'T'}$ (kW m^{-2})	Eddy momentum flux $\overline{u'v'}$ (cm^2 s^{-2})
420	−34.8	4.3
780	−26.5	0.7
1150	−9.5	0.3
2240	−2.1	0.8
3320	−3.1	1.9
Depth average	−11.3	1.6

These comparisons suggest that poleward eddy heat flux across the SAF is approximately the same size in Drake Passage and south of Australia, and that lower frequency fluxes are much stronger south of Australia.

The depth-averages of the profiles in Fig. 15b are

	AUSSAF	Northern Drake Passage	Southeast of New Zealand
All-frequency band	−40.6 (shear)	−26.9 (geographic)	−10.8 (geographic)
Eddy band	−11.3 (shear)	−15.4 (90-day)	

in units of kW m^{-2}, where the coordinate frame for each is indicated in parentheses. In the eddy band, northern Drake Passage experiences 25% larger poleward heat fluxes than AUSSAF, mainly due to larger near-surface values, and in spite of small equatorward deep fluxes. This difference partly reflects the difference between the 90-day coordinate frame used in Drake Passage and our daily varying coordinate frame since, when the 90-day frame does not well represent the daily direction of the stream, the alongstream velocity will be reduced in the 90-day frame and the cross-stream velocity will increase. For all frequency fluxes, those at AUSSAF are 33% larger than in northern Drake Passage. For com-

parison, the depth-average of all-frequency, geographic coordinate heat flux estimated by Bryden (1979) for central Drake Passage is 12.1 kW m^{-2} poleward—half that in the northern passage and one-third that at AUS-SAF. All-frequency poleward heat flux southeast of New Zealand is half that for northern Drake Passage and one-quarter that for AUSSAF.

The mean annual heat loss from the ocean south of the Polar Front is approximately 4.5×10^{14} W (Nowlin et al. 1985). Dividing by a pathlength of 20 000 km and a depth of 4 km, this corresponds to a pointwise heat flux of approximately 5.6 kW m^{-2}. Thus, poleward eddy heat fluxes estimated at all three sites are more than large enough to balance the observed loss (although those southeast of New Zealand are not statistically significant).

We have focused here on heat flux across the SAF, but in order for the heat to be delivered south of the Polar Front where it is required, it must cross the whole ACC. Estimates of poleward eddy heat flux averaged over all of Drake Passage give an indication of how much less heat is exchanged across the full ACC than across the SAF alone. Nowlin et al. (1985), using band-passed measurements, correcting for mooring motion, and working relative to the 90-day coordinate frame, found an average poleward eddy heat flux across Drake Passage in the 2 to 90 day band of 3.7 kW m^{-2}. This last figure is the best estimate available of the average eddy-band heat flux across the whole ACC and is one-quarter the size of the Nowlin et al. estimate of heat flux across the SAF alone. The size of the ACC-average flux is slightly smaller than the heat loss to be balanced, but the order of magnitude is correct and it is clear that eddy processes play a very important role in transporting heat across the ACC.

Although we believe that the comparisons made here are realistic, definitive statements about the relative size of eddy heat flux around the ACC and the implications for the global heat balance cannot be made until the current meter data from each of the ACC sites is treated identically, using the methods we have described for the AUSSAF data. That is, correcting for mooring motion, bandpassing, and working relative to a coordinate system that follows the daily change in orientation of the current stream.

c. Momentum flux

Time series of eddy and low-frequency momentum flux (not shown) appear similar to the heat flux time series. The quiet time at the beginning and end of the record is apparent. However, while the eddy heat flux values decrease dramatically below 1150 dbar, eddy momentum fluxes at 2240 and 3320 dbar (not shown) can be as large as for the shallower instruments. Low-frequency momentum fluxes are small below 1150 dbar, as they are for heat.

Figures 16a and 16b show profiles of mean cross-

stream eddy momentum flux for south-of-front and north-of-front conditions, respectively. The signs of the fluxes are somewhat indeterminate and their magnitudes are small compared with the benchmark 100 cm^2 s^{-2}, vertically and zonally averaged, estimated by Gill (1968) as that required to balance the momentum added to the ACC by the wind. Few of the momentum fluxes are statistically significant, but those that are indicate equatorward fluxes on the north side of the SAF act to decelerate the mean flow.

Our best estimate of the vertical profile of cross-stream eddy momentum flux (Table 6 and Fig. 16c) shows equatorward fluxes at all levels with a depth average of 1.6 cm^2 s^{-2}.

Since no significant eddy momentum fluxes were found in Drake Passage (Bryden 1979), the only in situ estimate in the ACC to compare with our results is that from southeast of New Zealand (Bryden and Heath 1985). We reproduce their profile in Fig. 16c (triangles) next to our all-frequency momentum flux profile (open circles). The depth averages of these are 27 cm^2 s^{-2} equatorward southeast of New Zealand and 4.5 cm^2 s^{-2} poleward at AUSSAF. We note in passing that in depth averaging eddy momentum flux, Bryden and Heath (1985) extended their 1000-m flux estimate to the sea surface since there were no shallower estimates available. We found that AUSSAF momentum fluxes calculated for all-frequency data had a maximum near 1000 m and smaller fluxes above; Bryden and Heath's vertical average may therefore be an overestimate.

All in situ estimates of eddy momentum flux are small enough to conclude that lateral divergence of eddy momentum flux does not play a significant role in the overall momentum balance of the ACC. This result is supported by satellite altimeter data and numerical models, as discussed in section 1.

d. Zonal momentum balance or meridional mass balance

Interfacial form stress,

$$\mathrm{IFS} = \rho_o f \frac{\overline{v'T'}}{\overline{\theta_z}} \qquad (3)$$

represents a vertical transfer of zonal momentum and is proportional to meridional eddy heat flux, $\overline{v'T'}$, so that poleward eddy heat flux implies downward flux of eastward momentum (Johnson and Bryden 1989). Here, ρ_o is a representative water density ($=1035$ kg m^{-3}), f is the Coriolis parameter, and $\overline{\theta_z}$ is the mean vertical gradient of potential temperature.

We have shown (section 4) that meridional eddy momentum fluxes are small and of indeterminate sign so that lateral divergence of eddy momentum flux is insufficient to close the Southern Ocean momentum balance, a result consistent with other observations (Bryden and Heath 1985; Morrow et al. 1994). Since meridional eddy heat fluxes are strong and poleward (Fig. 15), then
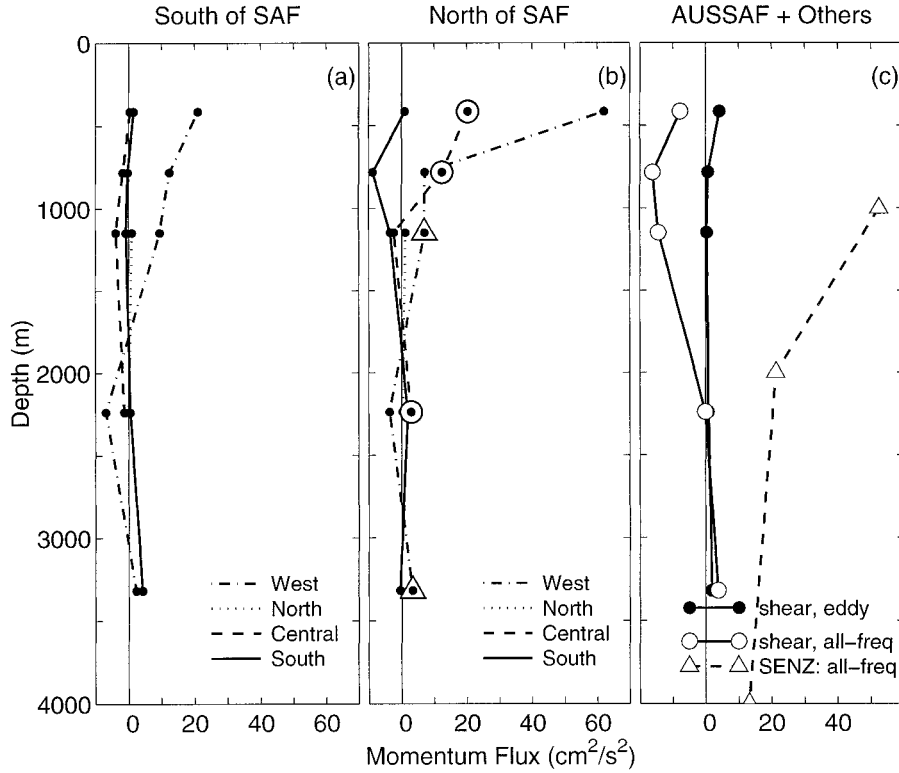
FIG. 16. Profiles of cross-stream eddy momentum flux, $\overline{u'v'}$. (a) Four AUSSAF moorings, shear coordinate, bandpassed data. Time averaging is done only for periods when array is south of SAF (see text for definition). Symbols over the data point indicating statistical significance are triangle = 90% and circle = 95%. (b) As for (a) but north of SAF. (c) As for Fig. 15b.

by (3) interfacial form stress must be large and downward, providing an alternative mechanism to balance the wind stress.

The zonal momentum balance averaged on isopycnals is a balance between the meridional flux of quasigeostrophic potential vorticity (or the difference of lateral divergence of eddy momentum flux and vertical divergence of interfacial form stress) and the vertical divergence of frictional stress,

$$\overline{v'q'} = -\frac{\partial}{\partial y}\overline{u'v'} + f\frac{\partial}{\partial z}\frac{\overline{v'T'}}{\overline{\theta_z}} = \frac{-\tau_z}{\rho_o}. \quad (4)$$

Johnson and Bryden (1989) argued that lateral divergence of eddy momentum flux was likely to be small and that, assuming frictional stress below the Ekman layer is negligible, interfacial form stress exactly balances the wind stress, carrying the wind input momentum downward undiminished to the level of topography where it is dissipated by bottom form stress.

We use the South mooring data to assess the vertical distribution of IFS since this has eddy heat fluxes significant at 95% at all levels and is therefore more likely to reveal the true vertical structure of IFS. Table 7 shows cross-stream eddy heat flux and IFS in shear coordinates for all-frequency and bandpassed data on the South

mooring. Also shown is the mean vertical temperature gradient from CTD data.

The bandpassed IFS is virtually constant with depth at approximately 0.2 N m^{-2}, roughly the same size as the mean wind stress over the ACC, supporting the theory of Johnson and Bryden (1989). The all-frequency IFS, however, shows a factor of 2 decrease between 1150 and 2240 dbar with values constant above and below this layer.

For a steady state, the eddy potential vorticity flux is proportional to the residual meridional circulation, $\overline{v}^*$, and

$$\overline{v'q'} = -f\overline{v}^* \quad (5)$$

[see Holton (1992) for a complete discussion]. In the absence of significant lateral divergence of eddy momentum flux

$$\overline{v}^* = \frac{-1}{\rho_o f}\frac{\partial \text{IFS}}{\partial z}, \quad (6)$$

and the observed divergence of IFS from the low-frequency motions drives a northward residual flow of order 1 mm s^{-1}.

The sense of this meridional flow is opposite to that inferred indirectly from observations, and in models.

TABLE 7. Interfacial form stress, $\rho_o f \overline{\hat{v}'T'}\,\theta_z$ at the South mooring for two frequency bands in shear coordinates. Positive stress indicates a downward flux of eastward momentum. Also shown is the cross-stream eddy heat flux and the mean vertical temperature gradient estimated from CTD data.

Pressure (dbar)	$\overline{\theta}_z$ (°C m^{-1})	All-frequency		Bandpassed	
		$\overline{\hat{v}'T'}$ (°C cm s^{-1})	IFS (N m^{-2})	$\overline{\hat{v}'T'}$ (°C cm s^{-1})	IFS (N m^{-2})
420	0.62×10^{-2}	-2.26	0.42	-1.09	0.21
780	0.58×10^{-2}	-2.40	0.48	-0.86	0.17
1150	0.23×10^{-2}	-1.00	0.51	-0.45	0.23
2240	0.08×10^{-2}	-0.13	0.20	-0.08	0.12
3320	0.07×10^{-2}	-0.19	0.31	-0.14	0.22

For example, Speer et al. (2000), using CTD data along WOCE transect SR3 and a simple parameterization of the eddy potential vorticity flux, inferred a southward eddy-driven mass flux in deep layers spanning Upper Circumpolar Deep Water and Antarctic Intermediate Water. They suggest the eddy-induced advection may account for up to half the southward flow required to balance the northward Ekman transport, with the remainder accomplished by deep geostrophic flow. Stevens and Ivchenko (1997) describe the residual mean streamfunction and IFS from the FRAM model. They find the largest contributor to the downward transfer of zonal momentum is the standing eddies, whose contribution to IFS increases with depth to drive a southward flow. Our estimates of IFS from current meter data do not include the standing eddy contribution, and we speculate that the northward flow driven by transient motions with period longer than 90 days would be more than compensated by divergence of standing eddy IFS of opposite sign.

Estimates of IFS (not bandpassed) in central Drake Passage (Johnson and Bryden 1989) were also downward but were roughly twice as large as our estimates due to a much weaker temperature gradient above 1500 m. IFS in Drake Passage also decreased by a factor of about 2 from shallow to deep instruments. Southeast of New Zealand (Bryden and Heath 1985), the vertical temperature gradient is similar to that for AUSSAF but meridional heat fluxes were of variable sign and not significantly different from zero so nothing can be inferred about IFS there.

5. Eddy energy distribution

Satellite maps of velocity variance (e.g., Morrow et al. 1994) indicate that eddy energy near the AUSSAF array is moderate but growing. In this section we estimate the amount of energy contained in the eddy field and the extent to which conversion of energy from the mean to eddy fields, or the reverse, is taking place.

a. Eddy kinetic energy

We have calculated eddy kinetic energy, EKE $= \frac{1}{2}(\overline{u'^2} + \overline{v'^2})$, using both shear and geographic coordinates, and found that both produce EKE profiles that are highly coherent across the array. The array mean profile for each coordinate system is shown in Table 8, and we note that geographic EKE is approximately twice as large as shear EKE. The two coordinate frames provide different views of eddy kinetic energy, both of which are meaningful. In shear coordinates, EKE is primarily a measure of velocity fluctuations associated with mesoscale eddy motions excluding variations in front orientation. In geographic coordinates, EKE measures the energy associated with all disturbances from the mean field with periods longer than 40 h. In both coordinate frames, 40% of EKE is contained in the 40 h–90 day band above 2500 m, and 70% below, with the remainder accounted for by low-frequency motions.

Sciremammano (1980) reported that "heat fluxing" events in central Drake Passage were associated with increases in EKE. We found the same link between heat

TABLE 8. Profiles of eddy kinetic energy in two coordinate frames, eddy potential energy, conversion of available potential energy in shear coordinates and eddy growth timescale.

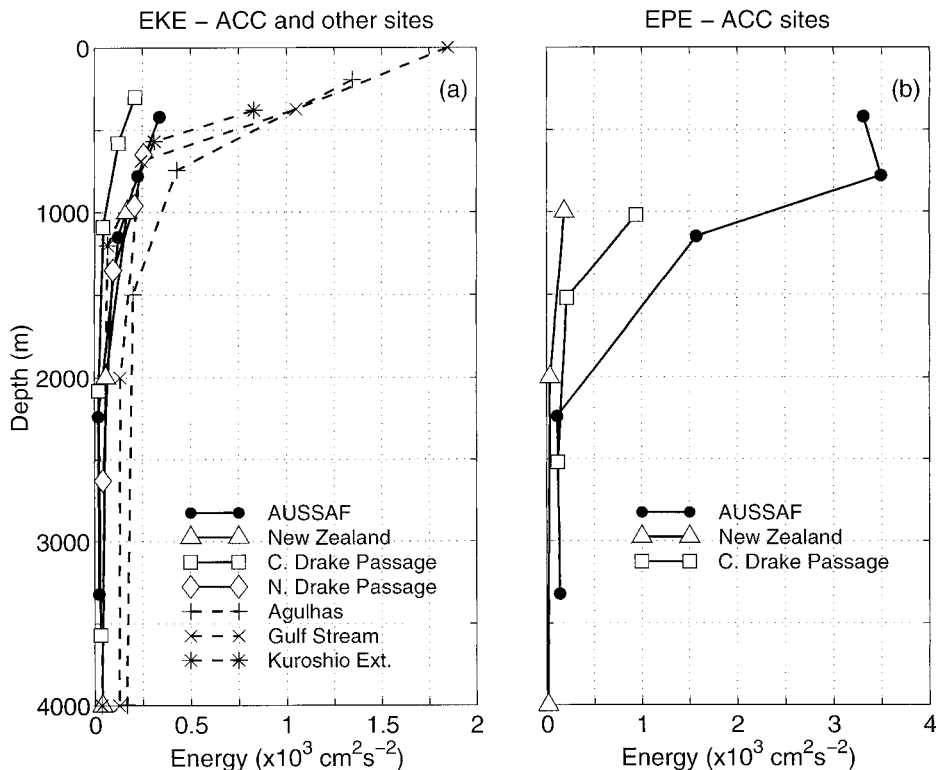| Pressure (dbar)	EKE $\frac{1}{2}(\overline{u'^2} + \overline{v'^2})$ (cm^2 s^{-2})		EPE $\frac{1}{2}g\alpha\overline{T'^2}/\theta_z$ (cm^2 s^{-2})	BC$_y$ $-g\alpha\,\overline{u'T'}\,\dfrac{\partial\overline{T}}{\partial y}\Big/\overline{\theta}_z$ (cm^2 s^{-3}) shear	Eddy growth time (days)
	Geographic	Shear			
420	339.0	136.2	3327.1	11.9×10^{-4}	33
780	223.7	97.7	3506.8	24.8×10^{-4}	17
1150	123.5	59.6	1579.1	10.7×10^{-4}	18
2240	18.2	12.7	112.3	0.4×10^{-4}	36
3320	23.6	21.5	140.6	0.7×10^{-4}	27

FIG. 17. Vertical profiles of (a) eddy kinetic energy $\frac{1}{2}(\overline{u'^2} + \overline{v'^2})$ and (b) eddy potential energy $\frac{1}{2}g\alpha\overline{T'^2}/\overline{\theta_z}$ for geographic coordinate, all-frequency AUSSAF data compared with profiles from other sites in the ACC: southeast of New Zealand and Drake Passage (all solid lines); and from western boundary current systems: Agulhas, Gulf Stream, and Kuroshio Extension (all dashed lines). Kinetic and potential energy for southeast of New Zealand and kinetic energy for central Drake Passage taken from Bryden and Heath (1985); potential energy for central Drake Passage is from Bryden (1979); kinetic energy for the remaining sites is from Schmitz (1996).

fluxes and EKE in geographic coordinates for all-frequency data, but not for shear coordinate, bandpassed data. We interpret these events as the passage of the front over the array.

Comparing the mean AUSSAF geographic EKE profile with those from other ACC and western boundary current (WBC) sites (Fig. 17a), we find that EKE south of Australia is approximately the same size as that southeast of New Zealand and in northern Drake Passage, while that in central Drake Passage is approximately half the size, above 2000 m. The Gulf Stream and Agulhas are more energetic than the ACC at all levels, except near 700 m in the Gulf Stream, and are particularly so above 500 m. The Kuroshio Extension is surface intensified like the other western boundary currents but more closely resembles the ACC at depth.

b. Eddy potential energy

Eddy potential energy, EPE $= \frac{1}{2}g\alpha\,\overline{T'^2}/\,\overline{\theta_z}$, is also highly coherent between moorings although it tends to be smaller at South where temperature variability is less than at the more northern moorings. Here, α is the effective thermal expansion coefficient

$$\alpha = -\frac{1}{\rho}\frac{d\rho}{dT} = -\frac{1}{\rho}\left(\frac{\partial\rho}{\partial T} + \frac{\partial\rho}{\partial S}\frac{dS}{dT}\right)$$

calculated from CTD data, g is gravitational acceleration, and $\overline{\theta_z}$ is the mean vertical gradient of potential temperature at the array (also from CTD). EPE is approximately an order of magnitude larger than EKE at all levels (Table 8), and since fluctuations in the 40 h–90 day band account for only 30%–40% of EPE, we suggest that most of the variability in the temperature field is due to the shifting orientation of the front and other events with periods longer than 90 days.

We compare the vertical profile of EPE at AUSSAF with estimates from central Drake Passage (Bryden 1979) and southeast of New Zealand (Bryden and Heath 1985), neither of which have data above 1000 m (Fig. 17b). Below 2000 m, EPE south of Australia is approximately the same as that in central Drake Passage and is three times as large as that southeast of New Zealand. Near 1000 m, AUSSAF levels are almost twice those in central Drake Passage and nine times those southeast of New Zealand. The northern Drake Passage was found to be much more energetic than the central passage in terms of EKE, and EPE there may also be

large. That EPE is much larger south of Australia than at the other ACC locations and is dominated by contributions from low-frequency events suggests that meandering of the front and other low-frequency motions are more common south of Australia than elsewhere in the ACC.

c. Energy conversion

Here we estimate three energy conversion terms that describe the exchange of kinetic and potential energies between the mean and eddy fields. They are the baroclinic conversion of potential energy available in the mean density field into eddy potential energy

$$\text{BC} = -\frac{g\alpha}{\overline{\theta}_z}\left(\overline{u'T'}\frac{\partial \overline{T}}{\partial x} + \overline{v'T'}\frac{\partial \overline{T}}{\partial y}\right), \qquad (7)$$

the barotropic conversion of energy from the mean velocity field into eddy kinetic energy

$$\text{BT} = -\left[\overline{u'u'}\frac{\partial \overline{u}}{\partial x} + \overline{u'v'}\left(\frac{\partial \overline{u}}{\partial y} + \frac{\partial \overline{v}}{\partial x}\right) + \overline{v'v'}\frac{\partial \overline{v}}{\partial y}\right], \quad (8)$$

and the production of mean kinetic energy by the eddies

$$\text{PKE} = -\left[\overline{u}\left(\frac{\partial}{\partial x}\overline{u'^2} + \frac{\partial}{\partial y}\overline{u'v'}\right) + \overline{v}\left(\frac{\partial}{\partial x}\overline{u'v'} + \frac{\partial}{\partial y}\overline{v'^2}\right)\right]. \qquad (9)$$

These terms are evaluated relative to the geographic coordinate frame, primarily because there is insufficient information to evaluate them in shear coordinates [without a more extensive analysis as in Hall (1991)], and second to aid comparison with energy conversion estimates in the literature.

In the equations, g is gravitational acceleration, α is the effective thermal expansion coefficient, $\overline{\theta}_z$ is the mean vertical gradient of potential temperature, and unit vectors $(\hat{x},\hat{y},\hat{z})$ are directed "eastward" (toward 104°T, across the main line of moorings), "northward" (toward 14°T, along the main line), and upward.

Marshall and Shutts (1981) describe the decomposition of the time-averaged heat flux field, in the mean equation for EPE, into a purely horizontally nondivergent component and a residual divergent component. The premise for this decomposition is that the nondivergent component of velocity, flowing along mean temperature contours, does not advect mean temperature; only the divergent component of the mean flow is responsible for the mean heat advection and therefore the baroclinic conversion events. By including eddy heat flux due to the nondivergent component of velocity in (7), BC can become misleading, indicating that baroclinic instability is occurring even when no heat advection occurs. Cronin and Watts (1996) optimally mapped their Gulf Stream velocity field, from current meters, to determine the geostrophic streamfunction from which they could estimate the nondivergent com-

ponent of eddy heat flux. They found that the incorporation of the nondivergent heat flux in (7) resulted in an overestimate of baroclinic conversion events by approximately a factor of 2. We are unable to make this calculation due to the limited spatial coverage of our array, but we bear in mind this result.

We can make a rough estimate of the horizontal gradients in (7), (8), and (9) by simple finite differences between pairs of moorings:

$$\frac{\partial}{\partial x} = \frac{\text{value at Central} - \text{value at West}}{\Delta x}$$

$$\frac{\partial}{\partial y} = \frac{\text{value at Central} - \text{value at South}}{\Delta y}$$

for $(\Delta x, \Delta y) = (52, 37)$ km. The conversion terms are evaluated at 1150 dbar, since this level has the best possible data on all moorings, for the common record length of 337 days. We find that

$$\text{BC} = (10.17 \pm 11.33) \times 10^{-4}\ \text{cm}^2\ \text{s}^{-3}$$

$$\text{BT} = (0.16 \pm 0.94) \times 10^{-4}\ \text{cm}^2\ \text{s}^{-3}$$

$$\text{PKE} = (-0.44 \pm 0.91) \times 10^{-4}\ \text{cm}^2\ \text{s}^{-3}.$$

The errors have been estimated from the standard errors of the 337-day mean velocity and temperature, variance of velocity and temperature, and momentum and heat fluxes for 17 degrees of freedom (corresponding to an integral timescale of 20 days).

The sign of BC is such that mean potential energy is converted to eddy potential energy. The magnitude of BC is likely an overestimate of the vigor of baroclinic conversion (by perhaps a factor of 2; Cronin and Watts 1996) since it includes a contribution from the horizontally nondivergent heat fluxes. Here BT indicates that kinetic energy is being transferred from the mean velocity field to the eddies, while PKE indicates eddies are producing mean kinetic energy; both are an order of magnitude less than BC. Although our estimates are uncertain due to limited spatial sampling, we conclude that the dominant energy conversion process is baroclinic conversion from available potential energy to eddy potential energy, with conversion between mean and eddy kinetic energy occurring at background levels. The net exchange between mean and eddy kinetic energy is BT − PKE = $(-0.28 \pm 0.9) \times 10^{-4}\ \text{cm}^2\ \text{s}^{-3}$ so that eddies lose kinetic energy to the mean flow, but at a rate 30 times lower than eddies gain potential energy from the mean density field.

d. Growth of eddies

The typical timescale for eddies to grow from zero to their average energy is the sum of their eddy energy divided by the sum of the energy conversion terms,

$$(\text{EKE} + \text{EPE})/(\text{BC} + \text{BT} - \text{PKE}) = 18\ \text{days}$$

at 1150 dbar. Bryden (1979) found eddy growth times

in Drake Passage to be 54 and 15 days at depths of 1020 and 2700 m, respectively, and suggested that the longer timescale is more representative of the timescale for growth of eddy motions since shallower depths probably dominate the contribution of eddy energy to the entire water column. This is certainly true for the AUS-SAF array, where EKE and EPE are large above 1150 dbar and decrease by an order of magnitude below.

Vertical information on energy conversion at the AUSSAF array is limited to the y component of baroclinic conversion,

$$\text{BC}_y = \frac{-g\alpha}{\overline{\theta_z}}\overline{v'T'}\frac{\partial \overline{T}}{\partial y} \qquad (10)$$

since only the cross-stream gradient of temperature is available at all instrument depths, estimated from CTD data along the main line of moorings. Spatial gradients using current meter data have gaps at some levels and cannot provide sufficient vertical resolution to interpret depth variations. Nevertheless, BC is the largest of the energy conversion terms and BC_y at 1150 dbar accounts for approximately half of BC. For the purpose of determining depth variations in energy conversion and eddy growth rate, we return to the shear coordinate frame since $\overline{v'T'}$ is vertically coherent and statistically significant at all levels only in shear coordinates.

Energy conversion varies more strongly with depth at the AUSSAF array (Table 8) than in Drake Passage where Bryden (1979) found BC_y to be 2.1×10^{-4} and 1.2×10^{-4} cm^2 s^{-3} at 1020 and 2700 m, respectively. Near 1000 m BC_y at AUSSAF is five times larger than in Drake Passage, but near 3000 m the two sites have similar conversion rates. Eddy growth timescale (Table 8), defined as

$$(\text{EKE}_{\text{shear}} + \text{EPE}_{\text{shear}})/\text{BC}_{y|\text{shear}},$$

is 18 days at 1150 dbar (in agreement with the geographic coordinate growth rate at 1150 dbar), increasing above and below this level to 30 days. We, therefore, conservatively estimate a typical timescale for eddies to grow from zero to their average energy level to be 30 days. This growth rate is about twice as fast as that in Drake Passage, consistent with the idea that the AUS-SAF array is in a region of growing eddy energy compared with the mature eddy field of Drake Passage.

6. Summary and conclusions

Current flow at the AUSSAF array is energetic, episodic, and highly variable with mean current speeds up to 33 cm s^{-1} and peaks up to 74 cm s^{-1} at 420 dbar. Mean current vectors turn across the array, consistent with a meander crest to the west of the array. SSH maps show that five meanders propagate slowly eastward during the deployment, occasionally stalling over the array for several months. Current vectors also rotate about the vertical coordinate, providing information on vertical motion at the array, which is of order 1 mm s^{-1}, similar

to that found in the Gulf Stream and Kuroshio Extension.

Fluctuations are vertically coherent and virtually in phase at all levels. There is a slight tendency for shallow temperature events to lead deep ones, while deep velocity events lead shallow by about 10°–20°C per 1000 m. Temperature fluctuations on the main line of moorings are in phase to within 1 day and West leads the main line by approximately 3 days. Features propagate across the array, on average, toward east-northeast with a speed of approximately 20 cm s^{-1}, nearly twice as fast as propagation speed southeast of New Zealand.

Typical integral timescales of fluctuations are approximately 20 days at and above 2240 dbar, similar to those found southeast of New Zealand, and 7 days at 3320 dbar. The reduction in timescale near the bottom is due to the increasing dominance of higher frequency processes there, which are likely a result of interactions with the bottom.

The definition of a daily varying coordinate frame that follows the direction of current flow allows the mesoscale variability of the SAF to be examined in isolation from the variability caused by the changing orientation of the front, and proves to be the best coordinate frame with which to assess meridional eddy fluxes of heat and momentum.

The unforeseen presence of a meander allowed us to examine the relationship between current flow and meander phase. We found that the relationship identified by Lindstrom et al. (1997) for the Gulf Stream was also applicable in the ACC: backing of the current, cold advection, and downwelling (veering, warm advection, and upwelling) occur in flow exiting (entering) a Southern Hemisphere meander crest.

Eddy heat fluxes across the SAF at AUSSAF are large (11.3 kW m^{-2} averaged over the array and vertically integrated), poleward, and significantly different from zero at the 95% confidence level. Zonally integrating this point estimate leads to a circumpolar eddy heat flux of 9×10^{14} W, more than enough to balance the estimated 4.5×10^{14} W lost south of the Polar Front. Including motions with periods longer than 90 days increases poleward heat flux to 33×10^{14} W, which is four times that found southeast of New Zealand and three times that found in Drake Passage. Results from Drake Passage suggest the amount of heat crossing the whole ACC may be only 25% of that crossing the SAF. Cross-stream eddy momentum fluxes are small, not statistically significant, and of indeterminate sign, but have a tendency for equatorward fluxes on the northern side of the SAF, and deceleration of the mean flow.

Interfacial form stress is downward and is large enough to balance the wind input momentum. It is constant with depth for eddy motions (periods 40 h–90 days), but decreases by a factor of 2 between 1150 and 2240 dbar for eddy and low-frequency motions combined (periods 40 h and longer). This divergence implies the existence of an eddy-induced northward flow in this

depth interval, driven by fluctuations with periods longer than 90 days. The northward flow is possibly compensated by divergence of the standing eddy component of IFS (not measured by the current meters), which was found to be large in FRAM, and of the sign to drive a southward flow (Stevens and Ivchenko 1997).

Eddy kinetic energy is similar in size to other ACC estimates, which are all smaller than EKE observed in western boundary currents. Eddy potential energy is an order of magnitude larger than EKE and is two times EPE in central Drake Passage and nine times that southeast of New Zealand above 1000 m. Below 1000 m, EPE at AUSSAF is the same size as that in central Drake Passage and three times that southeast of New Zealand. Most of this energy is contributed by low-frequency motions (periods longer than 90 days) so the large EPE values south of Australia suggest such motions are more common here than elsewhere in the ACC.

Baroclinic conversion is the dominant mechanism by which eddies grow south of Australia, with barotropic conversion an order of magnitude smaller. Baroclinic conversion is approximately five times larger than found in Drake Passage near 1000 m and approximately the same size near 3000 m. We estimate a typical timescale for eddy growth south of Australia to be 30 days—about twice as fast as in Drake Passage.

The site of the AUSSAF array is a region of growing eddy energy, in contrast to the mature eddy fields of Drake Passage and southeast of New Zealand. The strongest indication of this is the much larger eddy heat flux at AUSSAF and the correspondingly large baroclinic conversion of available potential energy. While the ACC remains sparsely monitored, the AUSSAF array provides new estimates of eddy variability in a region dynamically different to the sites previously monitored.

APPENDIX A

Correction for Mooring Motion

The mooring motion correction method of Hogg (1986, 1991) involves defining a canonical temperature profile that can best fit all recorded temperature profiles by the simple addition of a pressure offset to the (T, P) curves. Once the canonical profile is determined, temperature time series can be adjusted to any pressure level within the bounds of the canonical profile. This will only work when the isotherms at the array location are close to parallel. Pressure is required at only one level since all levels are assumed to be offset from each other by a constant pressure difference determined by the mooring design and additional pressure observations where available. Velocity can also be simulated by employing the thermal wind relation, requiring that the temperature–salinity $(T–S)$ relationship is well defined.

We have made two modifications to this method to better suit the ACC. The first is to assume a linear pressure offset, rather than a constant one, to infer deep pressures from the 420 dbar record. The second modification affects the velocity correction and deals with the fact that $T–S$ relationships in the Southern Ocean south of Australia are rarely tight. We avoid any assumption about the $T–S$ relationship by, instead, exploiting the tight relationship between specific volume anomaly (svan) and temperature in our study region, revealed in CTD data from WOCE section SR3. From this data we were able to define empirical functions for svan, $\delta_j = B_j(T)$ for $j = 1, 5$, one for each pressure range corresponding to a current meter level. The pressure range used to obtain enough (T, δ) pairs to fit a spline was 100 dbar above and below the adjusted levels of the current meter data (420, 780, 1150, 2240, and 3320 dbar). For each current meter level, svan may be assumed to be a function of temperature alone. We now write the thermal wind equations in terms of svan instead of density:

$$\frac{\partial u}{\partial z} = \frac{-g}{f(\delta + 1/\rho_p)}\frac{\partial \delta}{\partial y}; \qquad \frac{\partial v}{\partial z} = \frac{g}{f(\delta + 1/\rho_p)}\frac{\partial \delta}{\partial x} \quad \text{(A1)}$$

and infer velocity shear directly from svan. Here,

$$\delta = \frac{1}{\rho(S, T, P)} - \frac{1}{\rho_p}$$

and $\rho_p = \rho(35, 0, P)$.

We tested the inclusion of this second modification, and the mooring motion correction scheme itself, by withholding data at a particular level and simulating the withheld record by interpolating/extrapolating from data

above and below this record, as was done by Cronin et al. (1992). For the basic correction method, an interpolation (simulating 600-m data from 300 and 1000 m) gave rms differences between simulations and observations of about 0.4°C and 5 cm s^{-1}, and an extrapolation (simulating 300-m data from 600 and 1000 m) 0.5°C and 10 cm s^{-1}. By including the svan modification to the correction scheme we reduced the rms difference between velocity simulations and observations by a further 15%–20%. While these errors are not small, failure to correct for mooring motion produces larger ones. The 300-m instrument on the Central mooring was pushed below its resting level by 90 dbar on average, with a maximum depression of 450 dbar. In the thermocline, the vertical temperature gradient is 0.5°C/100 m, so not correcting for mooring motion could underestimate the temperature at the 300-m instruments by as much as 2.25°C and by 0.5°C on average. For periods where the mooring is in the front, correcting for mooring motion reduces the temperature variance by 20%. The consequences for eddy heat flux estimates of not removing mooring motion are severe; Nowlin et al. (1985) estimate eddy heat flux calculated from records contaminated by mooring motion are as much as 20% too large.

APPENDIX B

Calculation of Vertical Velocity

Hall (1986) and Lindstrom and Watts (1994), building on the work of Bryden (1980), describe a method for calculating vertical velocity, w, from temperature change and vertical rotation of horizontal velocity vectors as measured by a string of current meters. The method transforms the adiabatic heat equation (assuming negligible mixing)

$$\frac{\partial T}{\partial t} + u\frac{\partial T}{\partial x} + v\frac{\partial T}{\partial y} + w\frac{\partial \theta}{\partial z} = 0 \qquad \text{(B1)}$$

to

$$w = \frac{-\dfrac{\partial T}{\partial t} - \dfrac{\rho_o f}{g\alpha}\left(u\dfrac{\partial v}{\partial z} - v\dfrac{\partial u}{\partial z}\right)}{\dfrac{\partial \theta}{\partial z}} \qquad \text{(B2)}$$

using the thermal wind equation to write horizontal temperature gradients in terms of velocity shear. Here T is temperature; $\partial\theta/\partial z$ is the vertical potential temperature gradient; u, v, and w are velocity components in the x (eastward), y (northward), and z (upward) directions; f is the Coriolis parameter; g is the gravitational acceleration; ρ_o is the mean density; and α is the effective thermal expansion coefficient (as in section 5b).

As in appendix A for the mooring motion correction, we use the svan–T relationship instead of the traditional T–S to infer velocity shear from the thermal wind equa-

tion. Using thermal wind equations (A1) and separating variables in the partial derivatives

$$\left(\text{i.e., } \frac{\partial \delta}{\partial y} = \frac{\partial \delta}{\partial T}\frac{\partial T}{\partial y}\right)$$

leads to the expression of vertical velocity as

$$w = \frac{-\left[\dfrac{\partial T}{\partial t} + \dfrac{f\left(\delta + \dfrac{1}{\rho_p}\right)}{g\dfrac{\partial \delta}{\partial T}}\left(u\dfrac{\partial v}{\partial z} - v\dfrac{\partial u}{\partial z}\right)\right]}{\dfrac{\partial \theta}{\partial z}}. \qquad \text{(B3)}$$

The first term on the right-hand side is the contribution to the vertical velocity from local change of temperature, the second is that due to the advection of the temperature field, which we have written in terms of velocity shear. During times of strong vertical motion, w is dominated by the shear term and the local change term is not very different from times of weak vertical motion. Except for strong events, both terms are of similar magnitude. This indicates clearly that strong vertical motion is not due to residual mooring motion, which would show up as a peak in the local change term.

It is worth noting here that the choice of reference frame for the horizontal velocity components makes no difference to the vertical velocity calculation since in polar coordinates $u = R\cos\phi$ and $v = R\sin\phi$, where (R, ϕ) are current speed and direction measured anticlockwise from east, so

$$u\frac{\partial v}{\partial z} - v\frac{\partial u}{\partial z} = R^2\frac{\partial \phi}{\partial z}$$

and only the speed and the rotation of horizontal velocity vectors with depth are important.

Vertical derivatives ($\partial u/\partial z$, $\partial v/\partial z$, $\partial T/\partial z$) are approximated by a centered finite difference at adjacent current meters; u, v, T, δ, and ρ_p are averages of data at adjacent current meters; and the time change term is calculated as a second-order centered finite difference. The resultant vertical velocities therefore represent vertical motion between two current meters on the same current meter string and are nominally at the pressure midway between the current meters: 600, 965, 1695, and 2780 dbar.

REFERENCES

Belkin, I. M., 1990: Hydrological fronts of the Indian Subantarctic (in Russian with English abstract). *The Antarctic. The committee Reports,* Vol. 29, Nauka, 119–128.

Bryden, H. L., 1979: Poleward heat flux and conversion of available potential energy in Drake Passage. *J. Mar. Res., 37,* 1–22.

——, 1980: Geostrophic vorticity balance in midocean. *J. Geophys. Res., 85,* 2825–2828.

——, and R. D. Pillsbury, 1977: Variability of deep flow in the Drake

Passage from year-long current measurements. *J. Phys. Oceanogr.,* **7,** 803–810.

——, and R. A. Heath, 1985: Energetic eddies at the northern edge of the Antarctic Circumpolar Current. *Progress in Oceanography,* Vol. 14, Pergamon, 65–87.

Cronin, M., and D. R. Watts, 1996: Eddy–mean flow interaction in the Gulf Stream at 68°W. Part I: Eddy energetics. *J. Phys. Oceanogr.,* **26,** 2107–2131.

——, K. L. Tracey, and D. R. Watts, 1992: Mooring motion correction of the SYNOP Central Array current meter data. GSO Tech. Rep. 92-4, University of Rhode Island, 114 pp. [Available from University of Rhode Island, 215 South Ferry Rd., Narragansett, RI 02882.]

de Szoeke, R. A., and M. D. Levine, 1981: The advective flux of heat by mean geostrophic motions in the Southern Ocean. *Deep-Sea Res.,* **28A,** 1057–1085.

Gill, A. E., 1968: A linear model of the Antarctic Circumpolar Current. *J. Fluid Mech.,* **32,** 465–488.

——, J. S. A. Green, and A. J. Simmons, 1974: Energy partition in the large-scale ocean circulation and the production of mid-ocean eddies. *Deep-Sea Res.,* **21,** 449–528.

Gille, S. T., 1997: The Southern Ocean momentum balance: Evidence for topographic effects from numerical model output and altimeter data. *J. Phys. Oceanogr.,* **27,** 2219–2232.

Hall, M. M., 1986: Horizontal and vertical structure of the Gulf Stream velocity field at 68°W. *J. Phys. Oceanogr.,* **16,** 1814–1828.

——, 1989: Velocity and transport structure of the Kuroshio Extension at 35°N 152°E. *J. Geophys. Res.,* **94** (C10), 14 445–14 459.

——, 1991: Energetics of the Kuroshio Extension at 35°N, 152°E. *J. Phys. Oceanogr.,* **21,** 958–975.

Hogg, N. G., 1986: On the correction of temperature and velocity time series for mooring motion. *J. Atmos. Oceanic Technol.,* **3,** 204–214.

——, 1991: Mooring motion corrections revisited. *J. Atmos. Oceanic Technol.,* **8,** 289–295.

Holton, J. R., 1992: *An Introduction to Dynamic Meteorology.* 3d ed. Academic Press, 511 pp.

Inoue, M., 1985: Modal decomposition of the low-frequency currents and baroclinic instability at Drake Passage. *J. Phys. Oceanogr.,* **15,** 1157–1181.

Johnson, G. C., and H. L. Bryden, 1989: On the size of the Antarctic Circumpolar Current. *Deep-Sea Res.,* **36,** 35–53.

Le Traon, P. Y., F. Nadal, and N. Ducet, 1998: An improved mapping method of multi-satellite altimeter data. *J. Atmos. Oceanic Technol.,* **25,** 522–534.

Lindstrom, S. S., and D. R. Watts, 1994: Vertical motion in the Gulf Stream near 68°W. *J. Phys. Oceanogr.,* **24,** 2321–2333.

——, X. Qian, and D. R. Watts, 1997: Vertical motion in the Gulf Stream and its relation to meanders. *J. Geophys. Res.,* **102,** 8485–8503.

Marshall, J., and G. Shutts, 1981: On rotational and divergent eddy fluxes. *J. Phys. Oceanogr.,* **11,** 1677–1680.

McWilliams, J. C., W. R. Holland, and J. H. S. Chow, 1978: A description of numerical Antarctic Circumpolar Currents. *Dyn. Atmos. Oceans,* **2,** 213–291.

Morrow, R., R. Coleman, J. Church, and D. Chelton, 1994: Surface

eddy momentum flux and velocity variances in the Southern Ocean from Geosat altimetry. *J. Phys. Oceanogr.,* **24,** 2050–2071.

Munk, W. H., and E. Palmén, 1951: Note on the dynamics of the Antarctic Circumpolar Current. *Tellus,* **3,** 53–55.

Nowlin, W. D., Jr., and M. Clifford, 1982: The kinematic and thermohaline zonation of the Antarctic Circompolar Current at Drake Passage. *J. Mar. Res.,* **40** (Suppl.), 481–507.

——, and J. M. Klinck, 1986: The physics of the Antarctic Circumpolar Current. *Rev. Geophys.,* **24,** 469–491.

——, S. J. Worley, and T. Whitworth III, 1985: Methods for making point estimates of eddy heat flux as applied to the Antarctic Circumpolar Current. *J. Geophys. Res.,* **90,** 3305–3324.

Olbers, D., V. Gouretski, G. Seiß, and J. Schröter, 1992: *Hydrographic Atlas of the Southern Ocean.* Alfred Wegener Institute, 17 pp. and 82 plates.

Pedlosky, J., 1987: *Geophysical Fluid Dynamics.* 2d ed. Springer-Verlag, 710 pp.

Pillsbury, R. D., T. Whitworth III, W. D. Nowlin Jr., and F. Sciremammano Jr., 1979: Currents and temperatures as observed in Drake Passage during 1975. *J. Phys. Oceanogr.,* **9,** 469–482.

Rintoul, S. R., and J. L. Bullister, 1999: A late winter hydrographic section from Tasmania to Antarctica. *Deep-Sea Res.,* **46,** 1417–1454.

——, and S. Sokolov, 2000: Baroclinic transport variability of the Antarctic Circumpolar Current south of Australia (WOCE repeat section SR3). *J. Geophys. Res.,* in press.

——, J. R. Donguy, and D. H. Roemmich, 1997: Seasonal evolution of upper ocean thermal structure between Tasmania and Antarctica. *Deep-Sea Res.,* **44,** 1185–1202.

Schmitz, W. J., Jr., 1996: On the eddy field in the Agulhas Retroflection, with some global considerations. *J. Geophys. Res.,* **101,** 16 259–16 271.

Sciremammano, F., Jr., 1980: The nature of the poleward heat flux due to low-frequency current fluctuations in Drake Passage. *J. Phys. Oceanogr.,* **10,** 843–852.

Smith, W. H. F., and D. T. Sandwell, 1994: Bathymetric prediction from dense satellite altimetry and sparse shipboard bathymetry. *J. Geophys. Res.,* **99,** 21 803–21 824.

Speer, K., S. Rintoul, and B. Sloyan, 2000: The diabatic Deacon cell. *J. Phys. Oceanogr.,* **30,** 3212–3222.

Stevens, D. P., and V. O. Ivchenko, 1997: The zonal momentum balance in an eddy-resolving general-circulation model of the Southern Ocean. *Quart. J. Roy. Meteor. Soc.,* **123,** 929–951.

Thompson, R. O. R. Y., 1983: Low-pass filters to suppress inertial and tidal frequencies. *J. Phys. Oceanogr.,* **13,** 1077–1083.

Treguier, A. M., and J. C. McWilliams, 1990: Topographic influences on wind-driven, stratified flow in a β-plane channel: An idealized model for the Antarctic Circumpolar Current. *J. Phys. Oceanogr.,* **20,** 321–343.

Whitworth, T., III, W. D. Nowlin Jr., and S. J. Worley, 1982: The net transport of the Antarctic Circumpolar Current through Drake Passage. *J. Phys. Oceanogr.,* **12,** 960–971.

Wolff, J. O., E. Maier-Reimer, and D. J. Olbers, 1991: Wind-driven flow over topography in a zonal β-plane channel: A quasi-geostrophic model of the Antarctic Circumpolar Current. *J. Phys. Oceanogr.,* **21,** 236–264.